The VANDELS survey: a measurement of the average Lyman-continuum escape fraction of star-forming galaxies at $z = 3.5$

R. Begley [●],[1][★] F. Cullen [●],[1] R. J. McLure,[1] J. S. Dunlop,[1] A. Hall [●],[1] A. C. Carnall,[1]
M. L. Hamadouche,[1] D. J. McLeod,[1] R. Amorín [●],[2,3] A. Calabrò,[4] A. Fontana,[4] J. P. U. Fynbo,[5]
L. Guaita,[4,6] N. P. Hathi [●],[7] P. Hibon [●],[8] Z. Ji,[9] M. Llerena [●],[3] L. Pentericci,[4] A. Saldana-Lopez [●],[10]
D. Schaerer,[10] M. Talia [●],[11,12] E. Vanzella[13] and G. Zamorani[13]

[1]*Institute for Astronomy, University of Edinburgh, Royal Observatory, Edinburgh EH9 3HJ, UK*
[2]*Instituto de Investigación Multidisciplinar en Ciencia y Tecnología, Universidad de La Serena, Raúl Bitrán, 1305 La Serena, Chile*
[3]*Departamento de Física y Astronomía, Universidad de La Serena, Av. Juan Cisternas 1200 Norte, La Serena, Chile*
[4]*INAF – Osservatorio Astronomico di Roma, via Frascati 33, I-00078, Monteporzio Catone, Italy*
[5]*The Cosmic Dawn Center, Niels Bohr Institute, University of Copenhagen, Juliane Maries Vej 30, DK-2100 Copenhagen Ø, Denmark*
[6]*Núcleo de Astronomía, Facultad de Ingeniería, Universidad Diego Portales, Av. Ejército 441, Santiago, Chile*
[7]*Space Telescope Science Institute, 3700 San Martin Drive, Baltimore, MD 21218, USA*
[8]*European Southern Observatory (ESO), Vitacura, Casilla 19001, Chile*
[9]*Department of Astronomy, University of Massachusetts Amherst, 710 N. Pleasant Str, Amherst, MA 01003, USA*
[10]*Department of Astronomy, University of Geneva, 51 Chemin Pegasi, 1290 Versoix, Switzerland*
[11]*INAF – Osservatorio Astronomico di Bologna, Via P. Gobetti 93/3, I-40129 Bologna, Italy*
[12]*University of Bologna, Department of Physics and Astronomy (DIFA), Via Gobetti 93/2, I-40129 Bologna, Italy*
[13]*INAF – OAS, Osservatorio di Astrofisica e Scienza dello Spazio di Bologna, via Gobetti 93/3, I-40129 Bologna, Italy*

ABSTRACT

We present a study designed to measure the average Lyman-continuum escape fraction ($\langle f_{esc} \rangle$) of star-forming galaxies at $z \simeq 3.5$. We assemble a sample of 148 galaxies from the VANDELS spectroscopic survey at $3.35 \leq z_{spec} \leq 3.95$, selected to minimize line-of-sight contamination of their photometry. For this sample, we use ultra-deep, ground-based, U-band imaging and *Hubble Space Telescope* V-band imaging to robustly measure the distribution of $\mathcal{R}_{obs} = (L_{LyC}/L_{UV})_{obs}$. We then model the $\mathcal{R}_{obs}$ distribution as a function of $\langle f_{esc} \rangle$, carefully accounting for attenuation by dust, the intergalactic medium and the circumgalactic medium. A maximum likelihood fit to the $\mathcal{R}_{obs}$ distribution returns a best-fitting value of $\langle f_{esc} \rangle = 0.07^{+0.02}_{-0.02}$, a result confirmed using an alternative Bayesian inference technique (both techniques exclude $\langle f_{esc} \rangle = 0.0$ at $>3\sigma$). By splitting our sample in two, we find evidence that $\langle f_{esc} \rangle$ is positively correlated with Ly α equivalent width ($W_\lambda(\mathrm{Ly}\,\alpha)$), with high and low $W_\lambda(\mathrm{Ly}\alpha)$ subsamples returning values of $\langle f_{esc} \rangle = 0.12^{+0.06}_{-0.04}$ and $\langle f_{esc} \rangle = 0.02^{+0.02}_{-0.01}$, respectively. In contrast, we find evidence that $\langle f_{esc} \rangle$ is anticorrelated with intrinsic UV luminosity and UV dust attenuation; with low UV luminosity and dust attenuation subsamples both returning best fits in the range $0.10 \leq \langle f_{esc} \rangle \leq 0.22$. We do not find a clear correlation between f_{esc} and galaxy stellar mass, suggesting stellar mass is not a primary indicator of f_{esc}. Although larger samples are needed to further explore these trends, our results suggest that it is entirely plausible that the low dust, low-metallicity galaxies found at $z \geq 6$ will display the $\langle f_{esc} \rangle \geq 0.1$ required to drive reionization.

Key words: galaxies: fundamental parameters – galaxies: high-redshift – intergalactic medium.

1 INTRODUCTION

During the 'Epoch of Reionization' (EoR), the Universe underwent a phase change in which the hydrogen gas in the intergalactic medium (IGM) was transformed from its early cold neutral state into the largely ionized IGM we see around us today. Current data indicate that the EoR spanned the approximate redshift range from $z \simeq 10-15$ down to $z \simeq 5-6$ (Robertson et al. 2015; Bosman et al. 2021; Goto

et al. 2021; Robertson 2022). However, the detailed progress and physical drivers of reionization currently remain highly uncertain and somewhat controversial, with some evidence supporting a late, short-lived, rapid reionization process (e.g. Mason et al. 2018), while other indicators favour a more gradual evolution of the IGM, commencing at much higher redshift (e.g. Wu et al. 2021).

Historically, the two main candidates for producing the bulk of the LyC photon budget required to achieve hydrogen reionization have been active galactic nuclei (AGNs) and/or star-forming galaxies. However, with the number density of quasars and lower-luminosity AGN now known to fall rapidly at high redshift (Aird et al. 2015;

★ E-mail: rbeg@roe.ac.uk

McGreer et al. 2018; Parsa, Dunlop & McLure 2018; Kulkarni, Worseck & Hennawi 2019; Faisst et al. 2022), and recent constraints limiting the escape fraction of LyC photons in AGN to $f_{esc} \ll 1$ (Iwata et al. 2022), early star-forming galaxies are now thought to be the primary source of ionizing photons (Chary et al. 2016).

With ever improving measurements of the galaxy luminosity function at high redshift (Bowler et al. 2020; Harikane et al. 2022), it is becoming possible to track the progress of galaxy-driven reionization. However, doing so accurately requires reliable estimates of the production rate of LyC photons from early galaxies (e.g. Tang et al. 2019), and the average escape fraction ($\langle f_{esc} \rangle$) of such photons into the IGM (e.g. Ocvirk et al. 2021).

A number of studies have attempted to use measurements of the evolving UV luminosity density produced by the early star-forming galaxy population to estimate what the $\langle f_{esc} \rangle$ from young galaxies must be in order to deliver hydrogen reionization within the required time-frame (Robertson et al. 2013, 2015; Bouwens et al. 2015, 2021; Finkelstein et al. 2015, 2019). For example, Robertson et al. (2013) suggested that $\langle f_{esc} \rangle$ in the range of $10-20$ per cent is required, whereas the modelling of Finkelstein et al. (2019) concluded that $\langle f_{esc} \rangle \simeq 5$ per cent may suffice (helped by the gradual reduction in the optical depth τ to electron scattering derived from successive releases of data from Planck: now $\tau = 0.056 \pm 0.007$; Planck Collaboration VI 2020).

The inferred values for average $\langle f_{esc} \rangle$ quoted by such studies are inevitably dependent on a number of empirical results and model assumptions, such as the assumed ionizing photon production efficiency of early galaxies (e.g. Eldridge et al. 2017). One common additional assumption is that the production of LyC photons is dominated by the more numerous faint (and presumably metal poor) galaxies at such early times; however, alternative assumptions can be explored.

An example is presented in Naidu et al. (2020), who propose a model allowing f_{esc} to vary based on star formation rate surface density. In contrast to requiring a low-to-moderate $\langle f_{esc} \rangle$ across the entire galaxy population, their work suggests that $\gtrsim 80$ per cent of the ionizing photon budget may be accounted for by rarer, more massive galaxies with higher than average f_{esc}. Such uncertainties over the production and escape of LyC photons from EoR galaxies arise because direct measurements of the LyC emission from these objects are impossible. Therefore, with the aim of studying galaxies that are most directly analogous to those that drove reionization, many studies have focused on searching for LyC leakers at $3 \leq z \leq 4$, where the level of IGM transmission still allows the direct detection of LyC emission (Inoue et al. 2014).

Some of the earliest successes in such searches have come from deep rest-frame UV spectroscopy, both through targeted surveys such as KLCS (Steidel et al. 2018) and from serendipitous discoveries. The former has resulted in 13 secure detections of LyC emission (Pahl et al. 2021), including the LyC leaker Q1549-C25 first reported in Shapley et al. (2016). Other discoveries, both serendipitous and targeted, include such notable objects as *Ion 1-3* (Vanzella et al. 2012, 2016b, 2018; de Barros et al. 2016; Ji et al. 2020) and the Sunburst galaxy (Rivera-Thorsen et al. 2019; Vanzella et al. 2022). However, with less than 20 spectroscopically confirmed LyC leakers discovered to date at intermediate redshifts, the available sample of such sources remains small.

Constraints on the average escape fraction can also be derived from detailed analyses of larger samples that do not feature significant individual LyC detections, for example $\langle f_{esc} \rangle = 0.06 \pm 0.01$ (Pahl et al. 2021). However, even with relatively large samples of galaxies, it is still difficult to achieve robust constraints on the typical level of LyC flux at intermediate redshifts, as shown in the meta-analysis by Meštrić et al. (2021). Their work collates literature results from the last ~ 20 yr, finding that many studies were only able to derive upper limits on $\langle f_{esc} \rangle$, even from deep spectroscopic observations.

As a potentially efficient alternative to spectroscopic searches, a growing number of studies have sought to use narrow and/or broadband imaging to hunt for LyC emitting galaxies. The main observational requirement for such searches is the availability of deep *U*-band imaging, which a number of studies have obtained via programmes such as CLAUDS (Meštrić et al. 2020), and LACES (Fletcher et al. 2019), resulting in a number of likely LyC emitting candidates. As with spectroscopic studies, high angular-resolution imaging (effectively from *HST*) is required to robustly decontaminate samples of potential LyC leakers (Siana et al. 2015). Regardless of their ability to unveil new candidate LyC emitting galaxies, these deep *U*-band imaging surveys have generally only been able to place upper limits on $\langle f_{esc} \rangle$ across their full galaxy samples (e.g. Guaita et al. 2016; Grazian et al. 2017; Saxena et al. 2022).

In the past decade, a significant amount of effort has also been directed towards exploring which galaxy properties are correlated with, and therefore can be utilized as indirect indicators of, the level of leaking ionizing radiation. To date, the most promising such indicators for f_{esc} are tied to Lyα emission. Most recently, Pahl et al. (2021) confirmed the positive correlation between increased f_{esc} and Lyα equivalent width (W_λ(Lyα)), previously found by Steidel et al. (2018). This statistical link is physically supported by simulations, which show that both ionizing continuum flux and Lyα line emission can escape through the same ionized channels in the interstellar medium (ISM) (e.g. Kimm & Cen 2014; Wise et al. 2014).

However, the case for W_λ(Lyα) as a clean proxy for LyC leakage is not clear cut (e.g. Mostardi et al. 2013). With a host of properties able to alter the transmission of both Lyα and ionizing continuum photons, such as geometry and gas kinematics (Dijkstra, Gronke & Venkatesan 2016), any relationship between W_λ(Lyα) and f_{esc} is undoubtedly complex. Conflicting results also exist for the connection between other galaxy properties and f_{esc}, such as galaxy stellar mass and UV magnitude (e.g. Fletcher et al. 2019; Izotov et al. 2021; Pahl et al. 2021), both of which are particularly important in the ongoing debate over which galaxies provided the bulk of the ionizing photon budget in the EoR.

In addition to Lyα, a number of other rest-frame UV/optical spectral features, accessible by *JWST* for galaxies within the EoR, have been scrutinized as potential indicators of LyC leakage (Nakajima & Ouchi 2014; Katz et al. 2020; Ramambason et al. 2020; Mauerhofer et al. 2021). In particular, the usefulness of [O III] line emission from galaxies (W_λ([O III]) and the [O III]/[O II] ratio, hereafter O32), has been much explored, due to their association with recent bursts of star formation activity and increased ionizing photon production efficiency (Vanzella et al. 2016a; Izotov et al. 2018; Tang et al. 2019, 2021, 2022; Endsley et al. 2021). Indeed, more extreme [O III] properties are usually attributed to the presence of density-bounded H II regions (Kewley, Nicholls & Sutherland 2019), from which LyC photons are thought to escape (Jaskot et al. 2019). However, as with other proposed proxy indicators of LyC leakage, the link between W_λ([O III]), O32, and f_{esc} is not conclusive (e.g. Naidu et al. 2020; Saxena et al. 2022).

The analysis by Nakajima et al. (2020) suggests that high O32 is a requirement for high f_{esc}, but that not all galaxies with high O32 are necessarily LyC leakers (a situation that is mirrored by the relationship between O32 and Lyα emission; Tang et al. 2021). That no single measure has proven to be a clear and universal indicator of LyC leakage highlights the complexity of the underlying physics,

in which anisotropic or time-evolving leakage may play a significant role, potentially explaining apparently inconsistent results (Cen & Kimm 2015; Steidel et al. 2018; Fletcher et al. 2019). The lack of a clear consensus further bolsters the case for studying larger sample sizes with varied and complete data sets and/or using alternative methodologies (see also Tanvir et al. 2019; Meyer et al. 2020, for constraints derived using gamma-ray bursts and galaxy-IGM cross-correlations, respectively).

To try to advance this situation, in this study we have assembled a large sample of star-forming galaxies at $3.35 \leq z_{spec} \leq 3.95$ from the ultra-deep VANDELS spectroscopic survey (McLure et al. 2018b; Pentericci et al. 2018; Garilli et al. 2021). We utilize deep VLT/VIMOS U-band imaging to probe LyC emission ($\lambda_{rest} \simeq 820\,\text{Å}$), along with high resolution *HST* imaging to measure non-ionizing UV fluxes ($\lambda_{rest} \simeq 1300\,\text{Å}$) and effectively clean the sample from line-of-sight contamination. We have calibrated the imaging with additional astrometric corrections, and have undertaken sophisticated depth determinations to ensure that our derived photometric uncertainties are robust. We compare the observed distribution of ionizing to non-ionizing flux ratios with simulated ratios from a realistic model which is based on physically motivated and/or empirically measured inputs, and includes an accurate treatment of both IGM and circumgalactic medium (CGM) transmission via Monte Carlo sightline simulations. From this thorough analysis, for the first time via a broad-band imaging-based approach, we provide a statistical measurement ($\geq 3\sigma$) of the sample-averaged absolute escape fraction at $z \simeq 3.5$.

The paper is structured as follows. In Section 2, we describe the data sets used in this study, focusing on sample selection and cleaning, together with the additional calibration steps we have employed to extract robust photometry and accurately measure the LyC to non-ionizing UV flux ratios. In Section 3, we describe the construction of a model that can relate $\langle f_{esc} \rangle$ to the observed LyC to non-ionizing UV flux ratios, including the careful treatment of attenuation by dust, the IGM and CGM. Our constraints on $\langle f_{esc} \rangle$ for the full sample are presented in Section 4, where we also explore potential correlations between $\langle f_{esc} \rangle$ and Lyα equivalent width, UV luminosity, stellar mass and UV dust attenuation. We discuss the significance of our results in Section 5, before summarizing our conclusions in Section 6. Throughout the paper we adopt cosmological parameters $H_0 = 70\,\text{km}\,\text{s}^{-1}\,\text{Mpc}^{-1}$, $\Omega_m = 0.3$, and $\Omega_\Lambda = 0.7$. All magnitudes are quoted in the AB system (Oke & Gunn 1983), and unless otherwise stated, we refer to the absolute escape fraction as simply the escape fraction.

2 DATA AND SAMPLE SELECTION

The constraints on $\langle f_{esc} \rangle$ derived in this work fundamentally rely on accurately measuring the observed ratio of LyC to non-ionizing UV flux in a sample of star-forming galaxies at $z \simeq 3.5$.

The three key data sets necessary to perform this experiment are all publicly available. A suitable sample of spectroscopically confirmed star-forming galaxies has recently been provided in the CDFS by the final data release (DR4) of the VANDELS ESO public spectroscopic survey (Garilli et al. 2021). Moreover, the necessary measurements of the observed LyC flux are provided by the publicly available, ultra-deep, U-band imaging of the CDFS presented by Nonino et al. (2009). Finally, the necessary measurements of the non-ionizing UV flux are provided by the *HST* ACS F606W, hereafter V_{606}, imaging of the CDFS, released as part of version 2.0 of the Hubble Legacy Field programme[1] (Whitaker et al. 2019). In this section, we fully describe

the sample selection process, together with the steps taken to extract robust photometry from the ground-based and *HST* imaging.

2.1 The VANDELS survey

The sample of star-forming galaxies utilized in this work is drawn exclusively from the final data release (DR4) of the VANDELS ESO public spectroscopy survey (McLure et al. 2018b; Pentericci et al. 2018; Garilli et al. 2021). The VANDELS survey obtained ultra-deep (20-80 hours of integration), red optical ($4800 < \lambda_{obs} < 10200$ Å) spectra for a sample of 2087 galaxies with the VIMOS spectrograph on the VLT. The primary VANDELS sample, accounting for 83 per cent of the spectroscopic targets, consisted of galaxies on the star-forming main sequence (e.g. Daddi et al. 2007) within the redshift interval $2.4 \leq z_{phot} \leq 6.4$. Full details of the survey design can be found in McLure et al. (2018b), and a detailed description of the data reduction, data quality assurance, and spectroscopic redshift determinations can be found in Pentericci et al. (2018) and Garilli et al. (2021).

The initial sample selected for this work consists of 242 VANDELS DR4 star-forming galaxies within the CDFS,[2] with high-quality spectroscopic redshifts ($z_{flag} = 3$ or 4) within the interval $3.35 \leq z_{spec} \leq 3.95$. We note here that the spectroscopic redshifts for VANDELS galaxies with quality flags $z_{flag} = 3$ or 4 are derived from multiple spectral features and the analysis presented by Garilli et al. (2021) confirms that they are reliable at the 99 per cent level. Each galaxy had an associated stellar mass derived from multiwavelength broad-band photometry using the SED-fitting code BAGPIPES (Carnall et al. 2018, 2019) as described in Garilli et al. (2021), and a measured Lyα equivalent width ($W_\lambda(\text{Ly}\alpha)$) following the method outlined in Cullen et al. (2020) (following Kornei et al. 2010). The UV magnitude (M_{UV}) of each galaxy is calculated based on the VANDELS spectra and available photometry, following the method outlined in Section 3.3.

The low-redshift limit at $z_{spec} = 3.35$ was imposed to ensure that the U-band filter used for the VIMOS imaging only samples rest-frame wavelengths shortwards of the Lyman limit. In contrast, the high-redshift limit was determined based on a simulation of the combined impact of the IGM and CGM on the transmission of LyC photons. This indicated that $z_{spec} = 3.95$ was the redshift at which the increasing opacity of the IGM + CGM outweighed the improved signal-to-noise ratio provided by a larger sample size. We note that Vanzella et al. (2010a) reached the same conclusion regarding the optimal redshift window for detecting potential LyC emission in an earlier study using the same U-band imaging data.

2.2 Imaging data

This study makes use of the U-band imaging of the CDFS field obtained with VLT + VIMOS by Nonino et al. (2009) and the coincident V_{606} imaging obtained with *HST*. Fitting with the PSFEX software package (Bertin 2011) demonstrated that the point spread function (PSF) of the U-band mosaic shows little spatial variation. Over the area of the mosaic where the VANDELS star-forming galaxies are located, we find a median full width at half-maximum (FWHM) of 0.79 arcsec and a maximum FWHM of 0.80 arcsec. As a result, throughout this paper we measure photometry within circular

---

[1]

[2]A similar number of suitable VANDELS DR4 galaxies are available in the UDS survey field; however, the UDS currently lacks the necessary ultra-deep U-band imaging data.

apertures with a diameter of 1.2 arcsec in order to maximize the signal-to-noise ratio for compact sources (e.g. Brammer et al. 2016).

2.2.1 PSF homogenization

Our adopted method for determining $\langle f_{esc} \rangle$ relies on an accurate measurement of the LyC to non-ionizing UV flux ratio; effectively the $U-V_{606}$ colour. This measurement clearly relies on the U-band and V_{606}-band aperture photometry capturing the same fraction of total flux for each object. To meet this requirement, the V_{606} image was PSF homogenized to the U-band image using a convolution kernel generated by PHOTUTILS, based on stacks of isolated stars. Following PSF homogenization, a curve of growth analysis confirmed that the enclosed relative flux within an 1.2-arcsec diameter aperture on the U-band and V_{606}-band images matched to within ± 2 per cent.

2.2.2 Astrometry calibration

In addition to PSF homogenization, the measurement of an accurate $U - V_{606}$ colour requires any astrometric shifts between the U-band and V_{606}-band images to be minimized. To address this issue we selected a catalogue of bright sources, detected in both images with S/N $\geq 8\sigma$, with positions that matched within a tolerance of 0.5 arcsec. This catalogue revealed that the median astrometry offset between the two images was $\Delta\alpha = 0.133$ arcsec.

By applying a spatially varying correction to the U-band astrometry, based on the median off-sets of the nearest 200 bright objects, it was possible to reduce the median astrometry offset to $\Delta\alpha = 0.08$ arcsec. This improvement in astrometric accuracy allowed us to extract robust U-band photometry at the measured V_{606} centroids, without astrometric shifts contributing significantly to the uncertainty in the $U-V_{606}$ colours.

2.2.3 Sky subtraction and depth analysis

We adopted a two-step process to address the issues of sky subtraction and the positionally varying depth of the U-band imaging. The first step was to subtract a low-order, two-dimensional, sky-background fit to the U-band image with PHOTUTILS, using a dilated segmentation map to exclude objects from the fit. Following this global sky-subtraction, a second step was employed to deal with any remaining local variations. This step involved creating a dense grid of non-overlapping blank-sky apertures, each with a diameter of 1.2 arcsec. For each galaxy in our final sample, the U-band photometry was measured within an aperture with a diameter of 1.2 arcsec, centred on the measured V_{606} centroid, with the median flux of the nearest 200 blank-sky apertures taken as the local sky-background estimate. The corresponding value of σ_{MAD} measured from the flux distribution of the nearest 200 blank-sky apertures was adopted as the local 1σ depth estimate. An identical procedure was followed to measure and quantify the V_{606}-band photometry extracted from the PSF-homogenized V_{606} image.

A depth map, illustrating the spatial variation in sensitivity of the U-band image, is shown in Fig. 1. Within the region occupied by our final galaxy sample, we calculate a global median 1σ depth of $m_{1\sigma} = 30.4$. Although there is clearly spatial variation in the depth of the U-band image, ≥ 90 per cent of our final galaxy sample lie in regions with $m_{1\sigma} \geq 30.1$. Having an accurate measurement of the spatially varying depth allows us to allocate robust flux errors to each object as a function of their position.
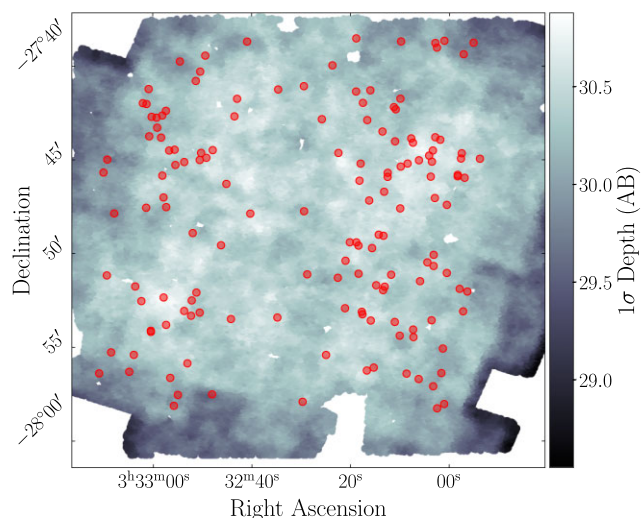

Figure 1. Depth map for the CDFS U-band mosaic, as measured within photometric apertures with a diameter of 1.2 arcsec. The locations of the 148 galaxies within our final star-forming galaxy sample are shown as filled red circles. Mapping the spatially varying depth allows robust photometric uncertainties to be allocated to each galaxy, based on its position.

2.3 Final sample selection

Unfortunately, the whole initial sample of 242 star-forming galaxies is not suitable for constraining the escape fraction of LyC photons, primarily due to the potential for significant contamination of the ground-based U-band photometry by flux from nearby companion objects. It was therefore necessary to clean our initial sample for potential contaminants, as described below.

2.3.1 Line-of-sight contamination in the imaging data

As discussed above, based on the $\simeq 0.8$ arcsec FWHM of the U-band PSF, we adopt photometric apertures with a diameter of 1.2 arcsec. Therefore, the first stage in cleaning the sample involved visually inspecting U-band cutouts of each object and removing all objects that displayed any level of contaminating flux from nearby companion objects within a radius of 0.6 arcsec. From the initial sample, 23 objects were excluded due to having U-band photometric apertures that were unambiguously contaminated by flux from nearby objects, leaving a sample of 219 remaining objects.

The second stage of the cleaning process exploited the high-spatial-resolution V_{606} imaging to identify small angular separation contaminants ($r < 0.6$ arcsec) that could not be identified from the low-spatial resolution U-band imaging. The third stage of the cleaning process made use of true-colour images constructed from the other available *HST* ACS imaging data (i.e. F435W, F775W, F850LP)[3] in order to exclude those extended objects that visually displayed strong colour gradients, potentially indicative of line-of-sight projections of objects at different redshifts. In total, based on the high-spatial resolution *HST* imaging, we excluded a further 34 objects, leaving a sample of 185 objects.

For a further 32 galaxies, it was not possible to state unambiguously that they contain no contaminating flux within the photometric aperture through a combination of the three previous cleaning stages.

---

[3]ACS F850LP and F606W imaging was available for all galaxies, with additional F775W and F435W imaging available for 70 per cent of the sample.

As a result, these galaxies were classed as *potentially* contaminated, and given our conservative approach, we also excluded these objects, leaving a sample of 153.

2.3.2 AGN contamination

The final stage of cleaning the sample involved excluding potential AGN. This process was based on the identification of sources within the 7Ms Chandra X-ray catalogue of the E-CDFS (Luo et al. 2017), which covers an area including the full VANDELS sample in the CDFS. We excluded a further five objects as potential AGN, all of which could be associated with high SNR detections in the 7Ms X-ray catalogue, within an angular separation of 1.1 arcsec.

2.3.3 Final galaxy sample

Following the exclusion of potential AGN, the final sample of galaxies consists of 148 star-forming galaxies within the redshift interval $3.35 \leq z_{\text{spec}} \leq 3.95$. Our conservative approach to cleaning excluded a total of 94 objects from the initial sample (39 per cent), primarily on the basis of potential photometric contamination from nearby objects. The redshift, stellar mass, and $W_\lambda(\text{Ly}\,\alpha)$ distributions of our final sample are shown in Fig. 2.

2.3.4 The LyC to non-ionizing UV flux ratio

As discussed previously, the observational constraint on f_{esc} for a given galaxy is derived from the LyC to non-ionizing UV flux ratio:

$$\mathcal{R}_{\text{obs}} = \left(\frac{L_{\text{LyC}}}{L_{\text{UV}}} \right)_{\text{obs}} = \left(\frac{\langle f_{\text{U}} \rangle}{\langle f_{\text{V}} \rangle} \right)_{\text{obs}}, \tag{1}$$

where $\langle f_{\text{U}} \rangle$ and $\langle f_{\text{V}} \rangle$ are the flux densities per unit frequency measured within 1.2-arcsec diameter apertures on the *U*-band and PSF-homogenized V_{606}-band images, respectively. In the next section, we describe the technique we have adopted to model the $\mathcal{R}_{\text{obs}}$ distribution of the final sample (see Fig. 3), and thereby measure the value of $\langle f_{\text{esc}} \rangle$. However, it is worth noting that it is $\mathcal{R}_{\text{obs}}$ that is the fundamental observable and that, after correcting for the effects of the IGM and CGM, it is $\mathcal{R}_{\text{obs}}$ that is directly related to a galaxy's total ionizing emissivity. The subsequent conversion between $\mathcal{R}_{\text{obs}}$ and f_{esc} is inevitably more model dependent, a fact that is worth re-membering when comparing the values of f_{esc} derived from different studies.

3 MODELLING THE $\mathcal{R}_{\text{obs}}$ PROBABILITY DISTRIBUTION

Armed with the $\mathcal{R}_{\text{obs}}$ distribution we can then proceeded to estimate $\langle f_{\text{esc}} \rangle$ for the final sample of 148 star-forming galaxies. To do this we first constructed a generative model to predict the probability distribution of $\mathcal{R}_{\text{obs}}$ for a given object, as a function of f_{esc}. The basic equation relating $\mathcal{R}_{\text{obs}}$ to f_{esc} is

$$\mathcal{R}_{\text{obs}} = f_{\text{esc}} \times \mathcal{R}_{\text{int}} \times e^{-\tau_\lambda^{\text{HI}}} \times 10^{0.4 A_{\text{UV}}}, \tag{2}$$

where $\mathcal{R}_{\text{int}}$ is the intrinsic LyC to non-ionizing UV flux ratio, $e^{-\tau_\lambda^{\text{HI}}}$ is the line-of-sight transmission through the IGM and CGM, and A_{UV} is the UV dust attenuation.[4]

---

[4]As measured at the rest-frame effective wavelength of the F606W filter, which is typically $\simeq 1300\,\text{Å}$ for our sample.
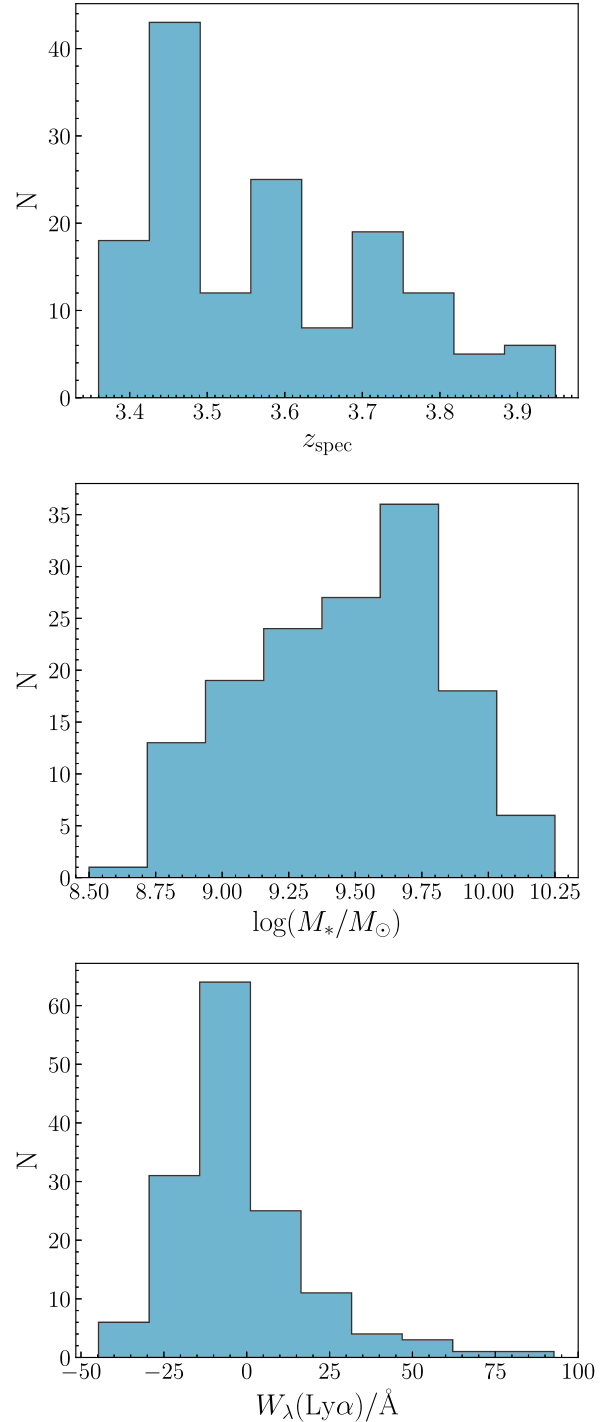
Figure 2. The distribution of spectroscopic redshift (top), stellar mass (middle), and Ly α equivalent width (bottom) for our final sample 148 of star-forming galaxies. The median values of the three properties shown are $z_{\text{spec}} = 3.58$, $\log(M_\star/M_\odot) = 9.5$, and $W_\lambda(\text{Ly}\alpha) = -6\,\text{Å}$ (see Section 4.3).

While $\mathcal{R}_{\text{int}}$ and A_{UV} can be estimated using standard stellar population fitting and/or empirical methods, the crucial complicating factor is the value of $e^{-\tau_\lambda^{\text{HI}}}$, which is strongly sight-line dependent and can take a range of values drawn from a highly non-Gaussian distribution (e.g. Steidel et al. 2018). As a result, there is no unique mapping between f_{esc} and $\mathcal{R}_{\text{obs}}$ for individual objects, and one must account for the full distribution of possible $\mathcal{R}_{\text{obs}}$ values at a given f_{esc}.
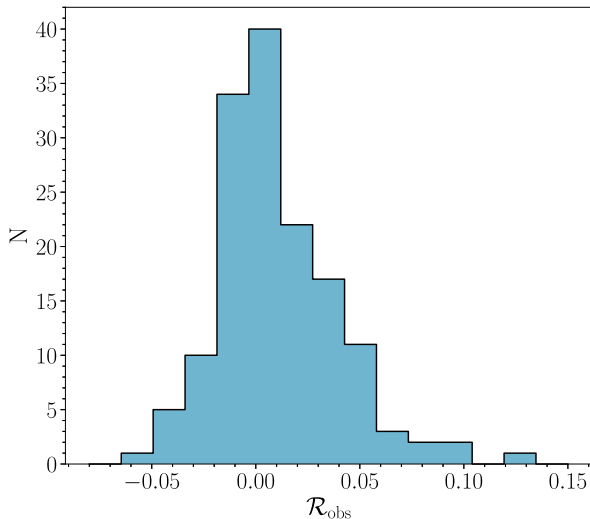
Figure 3. The $\mathcal{R}_{\rm obs}$ distribution of our final sample of 148 star-forming galaxies, derived in Section 2. It is the centroid and overall shape of this distribution that provides the fundamental observational constraint on $\langle f_{\rm esc} \rangle$.

In this section, we describe in detail how our model for $\mathcal{R}_{\rm obs}(f_{\rm esc})$ was constructed, focusing on each of the three key quantities ($\mathcal{R}_{\rm int}$, $e^{-\tau_\lambda^{\rm HI}}$, $A_{\rm UV}$) in turn.

3.1 Intrinsic LyC to non-ionizing UV flux ratio

The intrinsic LyC to non-ionizing UV flux ratio is determined by the properties of the underlying stellar population, which sets the shape of the intrinsic SED, and the galaxy redshift, which fixes the specific rest-frame wavelength regions covered by the U and V_{606}-band filters.

In order to define an intrinsic SED that is representative of the average properties of our sample, we first constructed a stack of the VANDELS spectra, following the method described in Cullen et al. (2019). The best-fitting stellar metallicity of this stacked spectrum was then determined by fitting the Binary Population and Spectra Synthesis version 2.2 (BPASSv2.2) SPS models (Eldridge et al. 2017; Stanway & Eldridge 2018) following the full spectral fitting approach outlined in Cullen et al. (2019), assuming a constant star formation history over a 100 Myr time-scale, binary stellar evolution, and a standard Kroupa (2001) IMF with an upper mass limit of $100 \rm M_\odot$. Our choice of the BPASS models was motivated by observations that suggest these models yield the best predictions for the ionizing continuum spectra of high-redshift stellar populations (e.g. Steidel et al. 2016; Reddy et al. 2022).

The best-fitting BPASS model had a metallicity of $Z_\star \simeq 0.001 \simeq 0.07 \rm Z_\odot$ (assuming Asplund et al. 2009), consistent with previous estimates of the average stellar metallicity of galaxies at similar redshifts and stellar masses (Cullen et al. 2019, 2021; Kashino et al. 2022). This best-fitting model was adopted as the representative intrinsic SED for our sample, and the individual $\mathcal{R}_{\rm int}$ values were then calculated by integrating through the U and V_{606}-band filters at the redshift of each galaxy. Across our final galaxy sample the individual values of $\mathcal{R}_{\rm int}$ range from 0.17 to 0.20 with a median value of $\mathcal{R}_{\rm int} = 0.19$. It is worth nothing that this is essentially the same intrinsic SED used to infer $\langle f_{\rm esc} \rangle$ and other related parameters in the recent the KLCS spectroscopic analyses at $z \sim 3$ (e.g. Steidel et al. 2018; Pahl et al. 2021).

3.2 IGM and CGM transmission

At the redshift of our sample, the nuisance parameter with the largest influence on the derived value of $\langle f_{\rm esc} \rangle$ is the optical depth of the IGM and CGM, which determines the transmitted fraction of ionizing photons through the intervening H I along the line of sight to each galaxy ($e^{-\tau_\lambda^{\rm HI}}$). The optical depth can vary significantly with sight line, depending on the exact distribution of neutral clouds (as a function of column density and redshift), and therefore must be accounted for in a probabilistic sense.

In many previous studies, it has been common to only consider the contribution of the IGM when accounting for H I optical depth (e.g. Vanzella et al. 2010a). However, as galaxies exist in regions of gas overdensities, and are known to be surrounded by significant quantities of H I in their CGM (out to $\simeq 700$ physical kpc; e.g. Rudie et al. 2012, 2013), sightlines to galaxies are not representative of random sightlines through the Universe. As a result, it is more accurate to account for *both* the IGM and CGM when considering the optical depth of H I towards galaxies (e.g. Steidel et al. 2018; Pahl et al. 2021).

To account for the IGM and CGM contributions, we generated transmission curves ($e^{-\tau_\lambda^{\rm HI}}$) using the parametrization for the column density and redshift distribution of H I clouds given in Steidel et al. (2018). Specifically, we generated 10 000 individual sightlines in six separate redshift bins ($z = 3.4, 3.5, 3.6, 3.7, 3.8, 3.9$), covering the full redshift range of our sample. Full details of the method used to generate the individual sightlines are provided in the Appendix, and examples of nine random sightlines at $z = 3.4$ are shown in the left-hand panel of Fig. 4, highlighting the significant variation.

For a given galaxy, a value of $e^{-\tau_\lambda^{\rm HI}}$ is obtained by selecting a random sight line at the nearest redshift and integrating through the U-band filter. The right-hand panel of Fig. 4 illustrates how the resulting distribution of $e^{-\tau_\lambda^{\rm HI}}$ is strongly peaked at zero, with a highly non-Gaussian shape.

3.3 UV dust attenuation

After the IGM + CGM transmission, the model parameter that has the largest systematic influence on the derived value of $\langle f_{\rm esc} \rangle$ is the UV dust attenuation. In this study, we have taken advantage of the rest-frame UV VANDELS spectra to adopt an empirical approach to calculating the level of UV attenuation on a galaxy-by-galaxy basis. By comparing to our adopted intrinsic SED model (see Section 3.1), which has a UV spectral slope of $\beta_{\rm int} = -2.44 \pm 0.02$, we calculated the value of $A_{\rm UV}$ for each object by measuring the observed UV spectral slope ($\beta_{\rm obs}$) from its VANDELS spectrum.

The first step in this process was fitting a power law ($f_\lambda \propto \lambda^\beta$) to each of the VANDELS spectra over the wavelength range of $1300-1800$ Å, within the continuum windows specified by Calzetti, Kinney & Storchi-Bergmann (1994). Fitting β in this fashion, the final galaxy sample has $\langle \beta_{\rm spec} \rangle = -1.26 \pm 0.04$, with a median value of $\beta_{\rm spec} = -1.29$. The average of these individual β estimates is fully consistent with the value derived from the stacked spectrum of the full sample ($\beta_{\rm stack} = -1.24 \pm 0.03$).

Armed with the individual values of $\beta_{\rm obs}$, it was then possible to calculate individual determinations of A_{1600} based on the value of $\Delta\beta = \beta_{\rm obs} - \beta_{\rm int}$. However, making this conversion requires a decision to be made on the form of the UV attenuation curve. Unfortunately, the average form of the UV attenuation curve at high redshift is still a matter of debate, with no consensus having been reached in the literature (e.g. Cullen et al. 2018; McLure et al. 2018b; Reddy et al. 2018; Shivaei et al. 2020), and we therefore
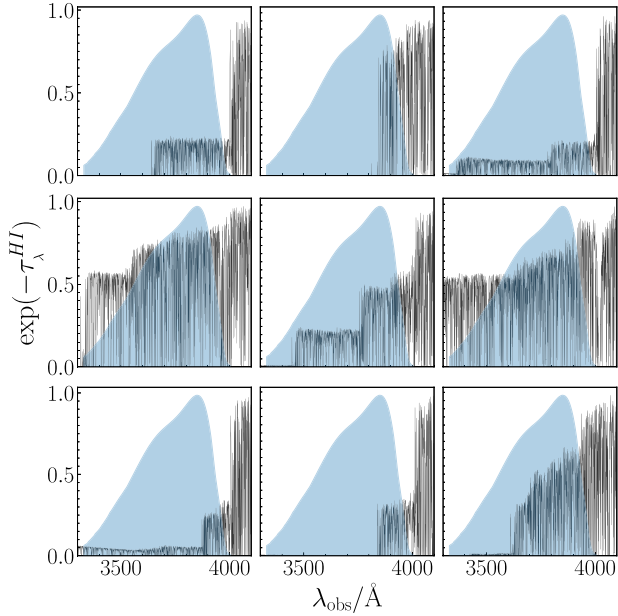
Figure 4. To accurately account for the fluctuating optical depth facing ionizing photons from a combination of the IGM and CGM, we generated a large number of individual sight-line transmission curves as a function of redshift, as detailed in Section 3.2. Left-hand panel: Nine random IGM + CGM transmission curves generated at $z = 3.4$ (black) over the observed wavelength range for LyC flux (the Lyman-limit lies at $\lambda_{\rm obs} = 4013$ Å at $z = 3.4$), illustrating the strong variation across different sightlines. The blue shading in the background of each panel shows the transmission of the U-band filter. Right-hand panel: Histograms showing the average transmission from 10 000 sightlines generated at $z = 3.55$, calculated by integrating the transmission curve for each sight line through the U-band filter. The filled grey histogram corresponds to sightlines accounting for *both* the IGM and CGM, while the red histogram shows IGM-only sightlines. The importance of incorporating the CGM contribution is highlighted by the significant increase in the relative number of sightlines with $\langle e_U^{-\tau}\rangle \simeq 0$. The inset panel shows the $\langle e_U^{-\tau}\rangle$ distribution of sightlines at $z = 3.4$ (green) and $z = 3.9$ (blue), highlighting the increasing optical depth at higher redshifts.

chose to employ a dust curve that is at least consistent with both the VANDELS spectra and our choice of intrinsic SED model. To do this, we fitted the stacked VANDELS spectrum using the BPASS intrinsic SED model, attenuated by a dust curve parameterized following Salim, Boquien & Lee (2018). According to this formulation, the Calzetti et al. (2000) attenuation curve is modified by a power-law exponent (δ), such that $\delta = 0.0$ corresponds to the Calzetti starburst curve and $\delta \simeq -0.5$ is close to the SMC extinction curve (e.g. Gordon et al. 2003). Fitting the stacked spectrum over the wavelength range of $1300-1800$ Å returned a best-fitting dust slope of $\delta = -0.25^{+0.37}_{-0.27}$, with no 2175 Å dust bump.

Based on this dust curve, we proceeded to convert the individual values of $\Delta\beta$ measured for each galaxy into attenuation at 1600 Å, using the relation: $A_{1600} = 1.28 \times \Delta\beta$. For each object, we then calculated the value of $A_{\rm UV}$ at the effective wavelength of the V_{606} filter using $A_{\rm UV} \simeq 1.2 \times A_{1600}$, where the constant has a slight redshift dependence. The error on $A_{\rm UV}$ ($\sigma_{A_{\rm UV}}$) was estimated by propagating the error on $\Delta\beta$.

3.4 Constructing model $\mathcal{R}_{\rm obs}(f_{\rm esc})$ distributions

Combining these three components, it is possible to construct the expected distribution of $\mathcal{R}_{\rm obs}$ as a function of $f_{\rm esc}$. The model distribution can then be statistically compared to the observed $\mathcal{R}_{\rm obs}$ distribution, to place constraints on $\langle f_{\rm esc}\rangle$ for any given sample. We adopted a Monte Carlo procedure for producing model $\mathcal{R}_{\rm obs}$ distributions as a function of $f_{\rm esc}$. For a set of $\mathcal{N}$ galaxies drawn from the full galaxy sample, we performed the following steps:

(i) For each galaxy, select a random IGM + CGM sight line at the appropriate redshift and calculate the value of $e^{-\tau_\lambda^{\rm HI}}$ integrated through the U-band filter.
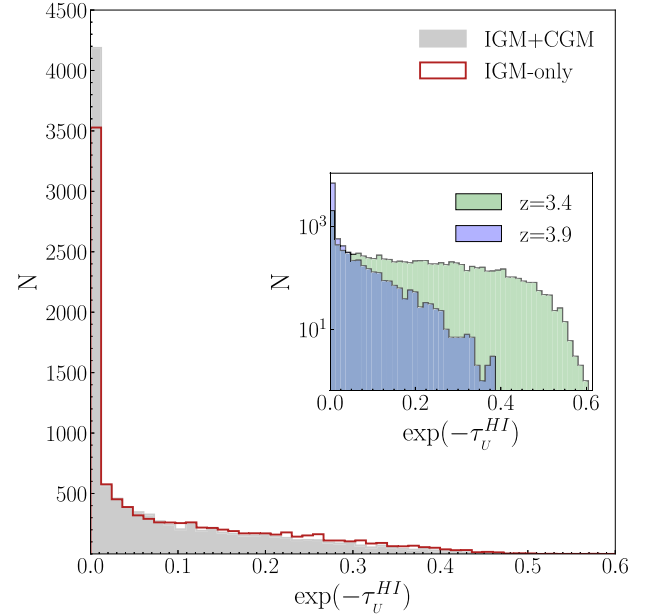
(ii) Set the value of $A_{\rm UV}$ by perturbing the measured value assuming a Gaussian scatter of $\sigma_{A_{\rm UV}}$ and ensuring that $A_{\rm UV} \geq 0$.

(iii) Using these two values, and the adopted value of $\mathcal{R}_{\rm int}$, calculate the expected $\mathcal{R}_{\rm obs}$ using equation (2).

(iv) Perturb $\mathcal{R}_{\rm obs}$ according to the depth of the U and V_{606}-band mosaics at the position of the galaxy.

These steps yield $\mathcal{N}$ model $\mathcal{R}_{\rm obs}$ values. The process was then repeated 10 000 times in order to build-up the average model distribution that could then be directly compared to the observed data, as shown in Fig. 5.

4 RESULTS

In this section, we describe how we estimated $\langle f_{\rm esc}\rangle$ for our final galaxy sample, using two approaches: (i) a binned maximum likelihood method and (ii) a Bayesian framework for combining individual $f_{\rm esc}$ estimates. We also explore whether trends in $\langle f_{\rm esc}\rangle$ can be identified by splitting our sample on the basis of properties that are expected to correlate with $f_{\rm esc}$; such as the equivalent width of Ly α, UV continuum slope β (a proxy for dust attenuation), galaxy stellar mass and intrinsic UV luminosity.

4.1 Maximum likelihood

The maximum likelihood technique is based upon a comparison between the observed and model $\mathcal{R}_{\rm obs}$ distributions. Model $\mathcal{R}_{\rm obs}$ distributions were built for a grid of $\langle f_{\rm esc}\rangle$ values between 0 and 1 with an interval of $\Delta\langle f_{\rm esc}\rangle = 0.001$, following the procedure outlined in Section 3. The fitting procedure was to maximize the following log-likelihood function:
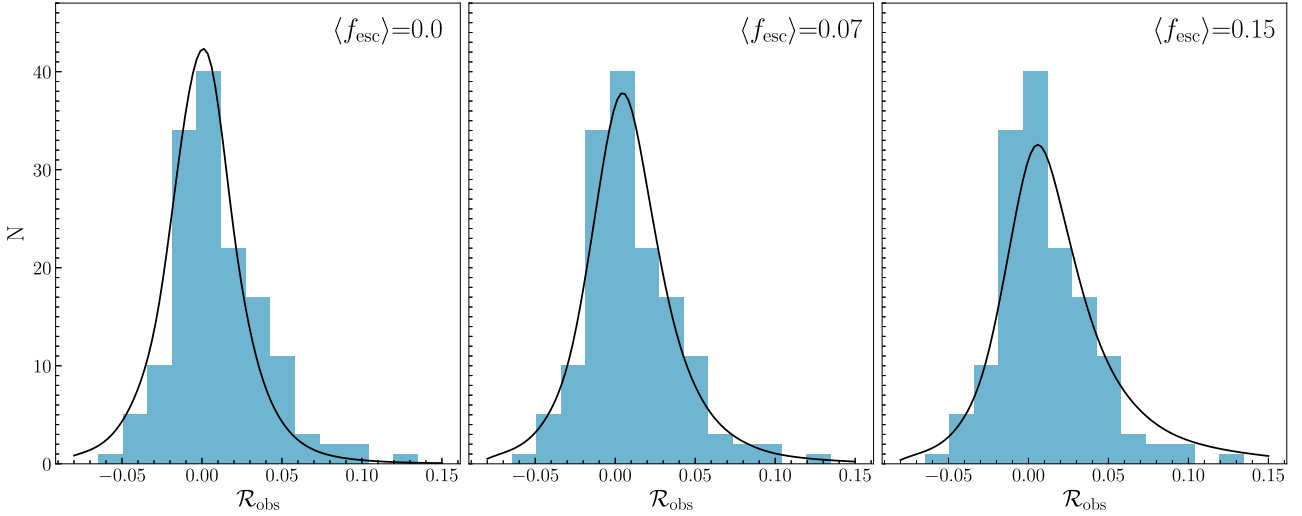
$$\ln \mathcal{L} = \sum_i n_i \ln p_i, \tag{3}$$

Figure 5. A comparison between the $\mathcal{R}_{obs}$ distribution for our full sample of 148 star-forming galaxies (blue) and the output of the model described in Section 3 (black line) for three different values of $\langle f_{esc} \rangle$. The best-fitting model returned by the maximum likelihood method described in Section 4.1 is shown in the middle panel, and corresponds to $\langle f_{esc} \rangle = 0.07 \pm 0.02$. It can be seen that the model predictions for $\langle f_{esc} \rangle = 0$ and $\langle f_{esc} \rangle = 0.15$ are not compatible with observed data, and both are formally excluded at $\geq 3\sigma$ (see Fig. 6).
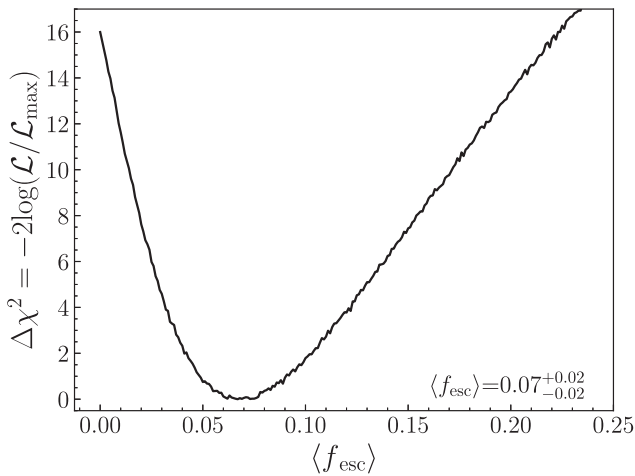
Figure 6. The result of the maximum likelihood fit to the $\mathcal{R}_{obs}$ distribution of the full sample of 148 star-forming galaxies. The best-fitting value is found to be $\langle f_{esc} \rangle = 0.07 \pm 0.02$ and $\langle f_{esc} \rangle = 0.0$ is excluded at $\geq 3\sigma$ confidence (i.e. $\Delta \chi^2 \geq 9$).

where the summation runs over the i bins of the $\mathcal{R}_{obs}$ histogram (see Fig. 3), n_i is the number of galaxies in bin i and p_i is the probability of finding a galaxy within bin i for a given value of f_{esc}. The probability p_i is naturally defined as n_i^m / N, where n_i^m is the number of galaxies in bin i predicted by the model, for a given f_{esc}, and N is the total number of galaxies in the sample ($N = 148$). The 1σ confidence interval can be estimated via

$$\Delta \chi^2 = -2 \ln \left(\mathcal{L} / \mathcal{L}_{max} \right) = 1, \qquad (4)$$

where $\mathcal{L}_{max}$ is the maximum likelihood value. Applying this technique we find clear evidence for a non-zero $\langle f_{esc} \rangle$ at the $>3\sigma$ level, with a best-fitting value of $\langle f_{esc} \rangle = 0.07 \pm 0.02$ (see Fig. 6).

Fig. 5 provides a visual illustration of this result. It can be seen from the middle panel that the model distribution corresponding to $\langle f_{esc} \rangle = 0.07$ provides an excellent description of the data. In contrast, the $\langle f_{esc} \rangle = 0$ model predicts too many galaxies with $\mathcal{R}_{obs} < 0$, while

the $\langle f_{esc} \rangle = 0.15$ model predicts a positive tail in excess of what is observed and underestimates the $\mathcal{R}_{obs} = 0$ peak.

4.2 Bayesian Inference

To complement the maximum likelihood fitting, we adopted a second approach for estimating $\langle f_{esc} \rangle$ that utilizes the individual posterior probabilities for f_{esc} of each galaxy. Using Bayes' theorem, the posterior probability for f_{esc} is given by

$$p(f_{esc} | \mathcal{R}_{obs}) \propto \int p(\mathcal{R}_{obs} | f_{esc}, \Theta) p(f_{esc}) p(\Theta) d\Theta, \qquad (5)$$

where $\Theta = (\mathcal{R}_{int}, e^{-\tau_U^{HI}}, A_{UV})$ and $p(\mathcal{R}_{obs} | f_{esc}, \Theta)$ is the likelihood for R_{obs}, $p(f_{esc})$ is the prior on the escape fraction, and $p(\Theta)$ is the prior on the additional free parameters. For a given galaxy, we can write the log-likelihood as

$$\ln p(\mathcal{R}_{obs} | f_{esc}, \Theta) = \frac{-(\mathcal{R}(f_{esc}, \Theta) - \mathcal{R}_{obs})^2}{2\sigma_{obs}^2} - \ln \left(\sqrt{2\pi} \sigma_{obs} \right), \qquad (6)$$

where σ_{obs} is the error on $\mathcal{R}_{obs}$ and $\mathcal{R}(f_{esc}, \Theta)$ is the predicted value of $\mathcal{R}$ for a given set of input parameters, according to equation (2).

The crucial aspect of the Bayesian approach then becomes determining the priors for each parameter. For simplicity, we assumed a fixed value for $\mathcal{R}_{int}$ for each galaxy (see Section 3.1). We adopted the following priors for each of the other three free parameters: (i) for f_{esc} we assume a uniform prior between 0 and 1; (ii) for A_{UV} we assume a Gaussian prior with mean and standard deviation given by the individual fits to the UV continuum slope of each galaxy (Section 3.3); (iii) finally, to generate a prior on $e^{-\tau_U^{HI}}$ we perform a kernel density estimation to turn the distribution of sightlines (see Section 3.2) into a smooth probability distribution. The resulting prior distributions for $e^{-\tau_U^{HI}}$ as a function of redshift are shown in Fig. 7.

Armed with the likelihood and prior distributions we determined the posterior of f_{esc} for each galaxy using an MCMC sampling technique (Foreman-Mackey et al. 2013). Examples of the posterior distributions for a detected (S/N $\geq 5\sigma$) and non-detected galaxy in the U-band are shown in the left-hand panel of Fig. 8. The value of
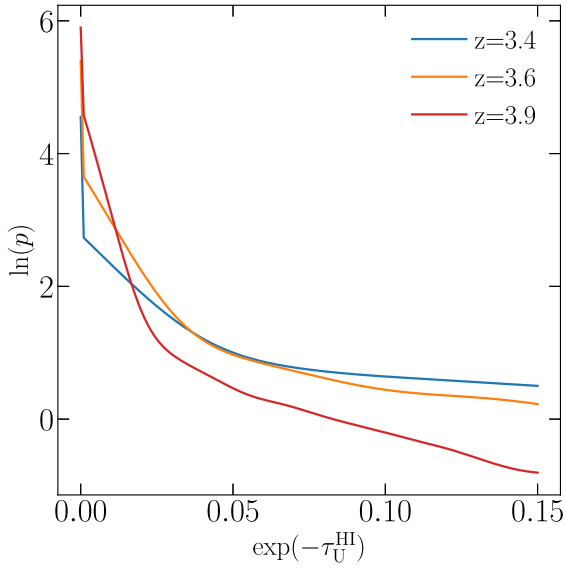
Figure 7. Probability density functions for $e^{-\tau_U^{HI}}$, used as priors in our Bayesian inference methodology (Section 4.2). To generate the smooth probability density functions we performed a kernel density estimation of the distribution of 10 000 sightlines at each redshift (examples of these can be seen in Fig. 4). The increase in probability density at low transmission (i.e. high IGM + CGM optical depth) with increasing redshift can clearly be seen.

$\langle f_{esc} \rangle$ can then be obtained by multiplying the individual posteriors:

$$p(\langle f_{esc} \rangle | \{R_{obs}\}) \propto \prod_i^{N_{gal}} p_i(f_{esc}). \qquad (7)$$

In the right-hand panel of Fig. 8, we show the resulting $p(\langle f_{esc} \rangle | \{R_{obs}\})$ for our full sample. It is important to note that equation (7) is only valid under that assumption that each galaxy has the same value of f_{esc}. Therefore, $\langle f_{esc} \rangle$ should be interpreted as the most likely value of f_{esc} assuming a uniform value across the sample, rather than the average of 148 individual (potentially different)

values. In this way, $\langle f_{esc} \rangle$ has the same physical interpretation as $\langle f_{esc} \rangle$ derived from the maximum likelihood fitting above. Using this method, we infer a best-fitting value of $\langle f_{esc} \rangle = 0.05 \pm 0.01$, fully consistent (within 1σ) with the value inferred from the maximum likelihood approach, and inconsistent with $\langle f_{esc} \rangle = 0$ at the $\geq 3\sigma$ level.

4.3 Escape fraction dependence on galaxy physical properties

Having established that $\langle f_{esc} \rangle$ for the full sample is non-zero, it is clearly of interest to investigate whether or not there is any indication that f_{esc} correlates with other galaxy properties. As discussed in the introduction, reliable proxies for LyC escape are required in order to infer f_{esc} during the reionization era, where direct measurements are not possible.

One of the most prominent amongst potential f_{esc} indicators is the equivalent width of the Ly α line ($W_\lambda(\text{Ly}\,\alpha)$), which is expected to correlate with LyC escape since both are sensitive to the column density and distribution of H I within galaxies (e.g. Gronke, Bull & Dijkstra 2015; Verhamme et al. 2015; Dijkstra et al. 2016). Observational evidence in support of this connection has recently been reported via spectroscopic analyses of galaxies at $z \simeq 3$, which find strong evidence for a correlation between f_{esc} and $W_\lambda(\text{Ly}\,\alpha)$ (Marchi et al. 2017; Steidel et al. 2018; Pahl et al. 2021), as well as $W_\lambda(\text{Ly}\,\alpha)$ and the covering fraction of H I (Reddy et al. 2016; Gazagnes et al. 2020; Reddy et al. 2022; Saldana-Lopez et al. 2022). Other likely indirect tracers of the neutral H I column density of galaxies include the dust content (traced by the UV continuum slope, β) and stellar mass ($M_\star$); indeed, both of these quantities are known to be linked to the escape of Ly α photons (Du et al. 2018; Cullen et al. 2020).

Finally, it is also of interest to investigate whether f_{esc} and UV luminosity are correlated, given that calculating the global ionizing background during the EoR typically relies on integrating {down the UV galaxy luminosity function with an assumption that f_{esc} is constant (e.g. Robertson et al. 2015). Below we explore the correlation between f_{esc} and each of these galaxy properties ($W_\lambda(\text{Ly}\,\alpha)$, β, $M_\star$, L_{UV}), in turn.
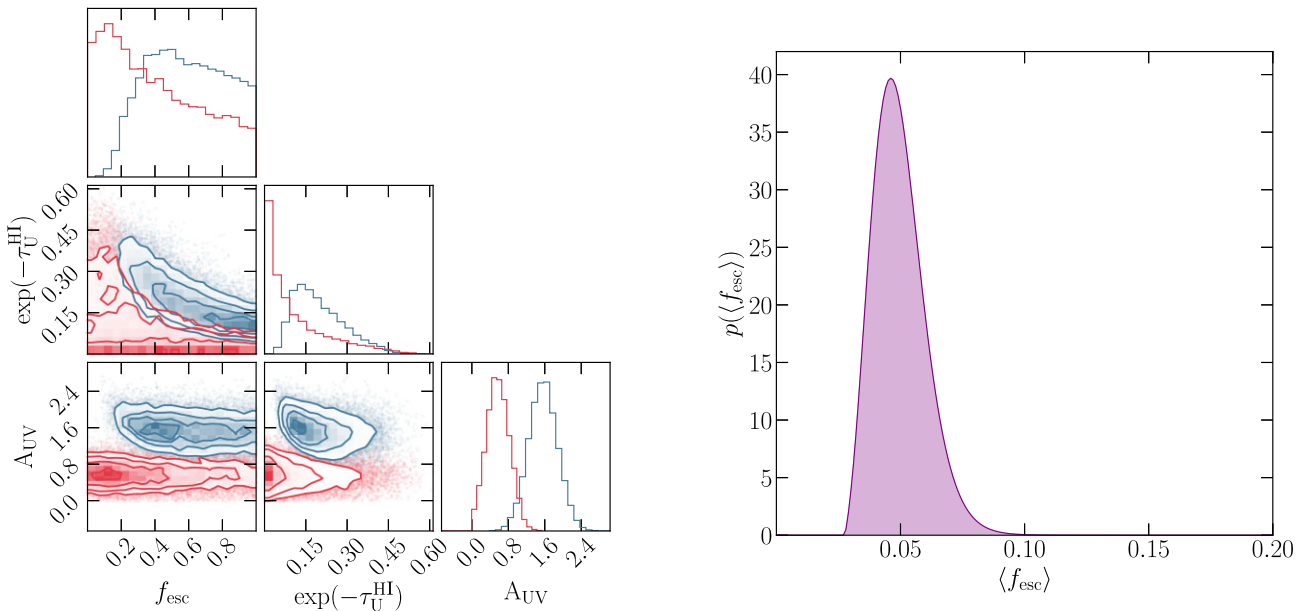

Figure 8. *Left*: A corner plot showing the 1D and 2D marginalized posteriors for f_{esc}, A_{UV} and $e^{-\tau_U^{HI}}$ for two example galaxies drawn from our final sample. The blue posteriors show one of the two galaxies in our full sample with a robust ($\geq 5\sigma$) individual $\mathcal{R}_{obs}$ detection. The red posteriors show an example of a typical galaxy that is not individually detected. To calculate the average $\langle f_{esc} \rangle$ for a given galaxy sample, the individual f_{esc} posteriors (i.e. curves in the upper left-hand panel) were multiplied together. *Right*: The posterior probability $p(\langle f_{esc} \rangle | \{R_{obs}\})$ for the full galaxy sample, corresponding to $\langle f_{esc} \rangle = 0.05 \pm 0.01$.
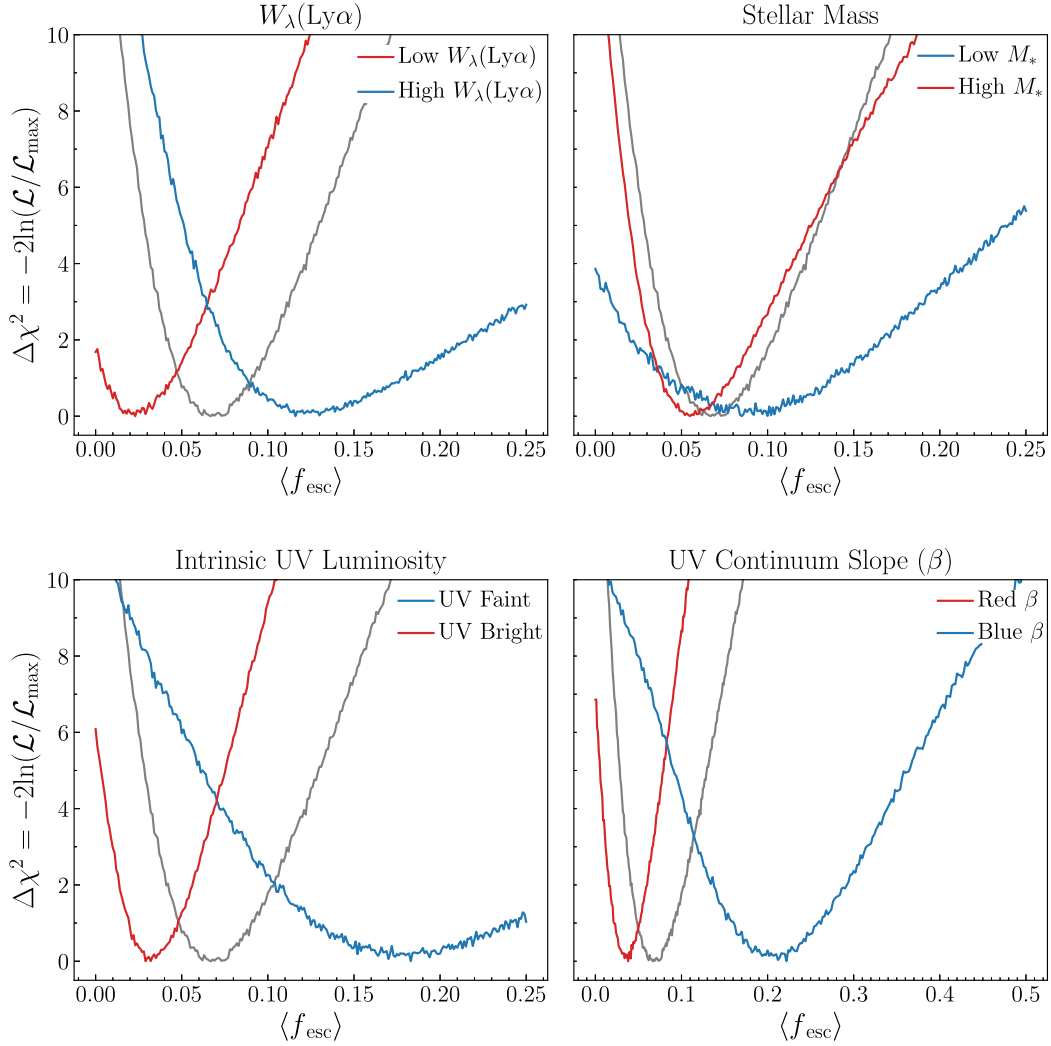
Figure 9. The constraints on $\langle f_{esc} \rangle$ returned by the maximum-likelihood technique for the four sample splits described in Section 4.3. In each panel, the red and blue curves show the $\langle f_{esc} \rangle$ constraints when the full sample is split in two at the median value of the physical parameter in question. The red and blue curves can be identified by the labels in the top-right corner of each panel. For reference, the grey curve in each panel shows the constraint on $\langle f_{esc} \rangle$ for the full galaxy sample.

4.3.1 $W_\lambda(Ly\alpha)$

To investigate the link between f_{esc} and $W_\lambda(Ly\alpha)$, we split the full sample in half at the median value of $W_\lambda(Ly\alpha) = -6$ Å. After excluding two galaxies with unreliable $W_\lambda(Ly\alpha)$ measurements due to artefacts in the VANDELS spectra, the resulting low− and high−$W_\lambda(Ly\alpha)$ sub-samples had median equivalent widths of $W_\lambda(Ly\alpha)=-14.2$ Å and $W_\lambda(Ly\alpha) = 4.9$ Å, respectively. Fitting the two sub-samples using the maximum likelihood technique returned best-fitting values of $\langle f_{esc} \rangle = 0.02^{+0.02}_{-0.02}$ for the low-$W_\lambda(Ly\alpha)$ sub-sample and $\langle f_{esc} \rangle = 0.12^{+0.06}_{-0.04}$ for the high-$W_\lambda(Ly\alpha)$ subsample (Fig. 9). Using the Bayesian inference methodology, the constraints for the low- and high-$W_\lambda(Ly\alpha)$ subsamples were $\langle f_{esc} \rangle < 0.03\,(2\sigma)$ and $\langle f_{esc} \rangle = 0.08^{+0.02}_{-0.02}$ (Fig. 10). These results represent significant evidence ($>3\sigma$) for an increase in f_{esc} with increasing $W_\lambda(Ly\alpha)$, in broad agreement with recent spectroscopic studies (Steidel et al. 2018; Pahl et al. 2021).

4.3.2 UV continuum slope

Next, we looked for a link between f_{esc} and the observed UV continuum slope β_{obs} (a proxy for dust attenuation at UV wavelengths). A

$f_{esc}-\beta_{obs}$ correlation is expected due to the sensitivity of LyC photon escape to the dust and H I column density of the ISM.

Again, the full galaxy sample was split in half at the median value of $\beta_{obs} = -1.29$, producing low attenuation ('blue', with median $\beta_{obs} = -1.62$) and high attenuation ('red', with median $\beta_{obs} = -0.92$) subsamples. Applying the maximum likelihood approach returned best-fitting values of $\langle f_{esc} \rangle = 0.22^{+0.04}_{-0.06}$ and $\langle f_{esc} \rangle = 0.04^{+0.01}_{-0.02}$ for the low- and high-attenuation sub-samples, respectively (Fig. 9). Similarly, the Bayesian inference approach returned $\langle f_{esc} \rangle = 0.14^{+0.06}_{-0.04}$ for the low-attenuation sub-sample and $\langle f_{esc} \rangle < 0.03\,(2\sigma)$ for the high-attenuation subsample (Fig. 10). Taken together, these results again represent significant evidence in favour of a picture in which galaxies with lower levels of UV dust attenuation display higher values of $\langle f_{esc} \rangle$.

4.3.3 Stellar mass

Although $W_\lambda(Ly\alpha)$ and β_{obs} are two galaxy properties with a clear and direct link to f_{esc}, it is also interesting to examine any correlation between f_{esc} and stellar mass, a property that is already know to correlate with both $W_\lambda(Ly\alpha)$ and UV dust attenuation (e.g McLure et al. 2018b; Cullen et al. 2020). Splitting the sample into low-
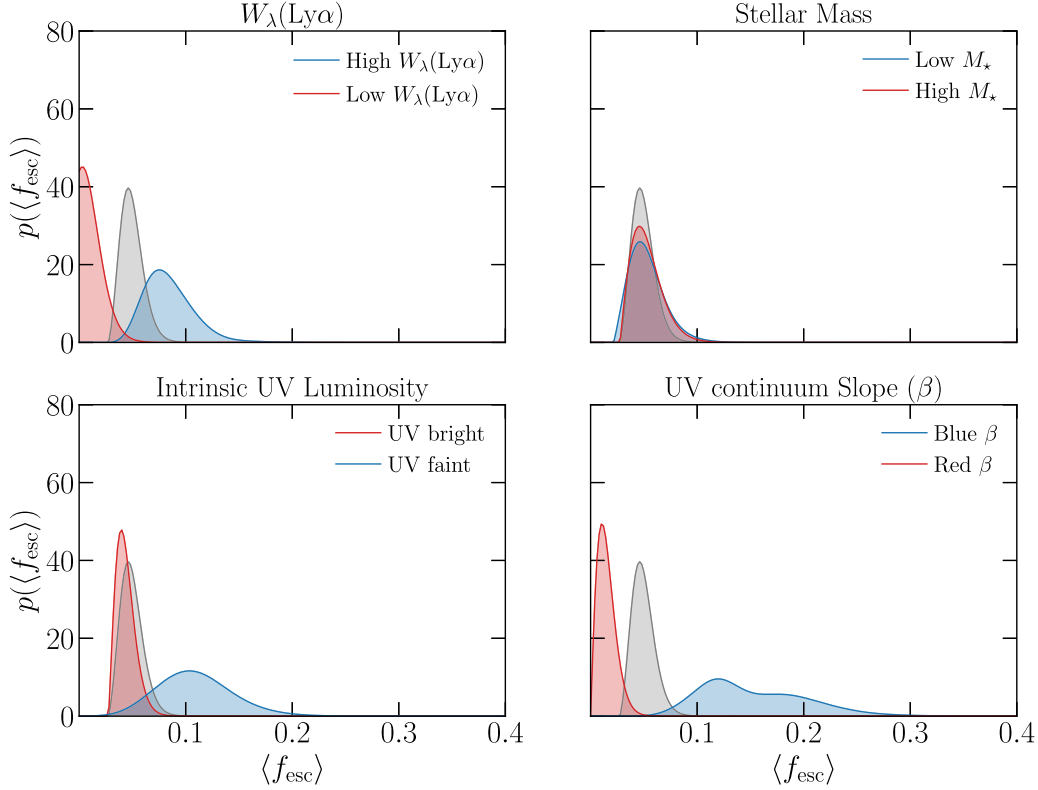
Figure 10. The constraints on $\langle f_{esc} \rangle$ returned by the Bayesian inference technique for the four sample splits described in Section 4.3 in the same format as Fig. 9. The red and blue curves show the posterior probability distributions for the sample splits, whereas the grey curve in each panel shows the posterior probability distribution of $\langle f_{esc} \rangle$ for the full sample. As before, the red and blue curves can be identified by the labels in the top-right corner of each panel.

$M_\star$ (median $= 10^{8.72} M_\odot$) and high-$M_\star$ (median $= 10^{9.22} M_\odot$) subsamples, the maximum likelihood approach returned best-fitting values of $\langle f_{esc} \rangle = 0.09^{+0.05}_{-0.04}$ and $\langle f_{esc} \rangle = 0.06^{+0.02}_{-0.02}$, respectively (Fig. 9). With our Bayesian inference approach, we derive corresponding constraints of $\langle f_{esc} \rangle = 0.05^{+0.02}_{-0.01}$ and $\langle f_{esc} \rangle = 0.05^{+0.02}_{-0.01}$ (Fig. 10). In either case, we find that any dependence of f_{esc} on $M_\star$, if one exists, is not a strong as the dependence on $W_\lambda(Ly\,\alpha)$ and β, suggesting that $M_\star$ is at best a secondary indicator of f_{esc}.

4.3.4 Intrinsic UV luminosity

Finally, we divided the full galaxy sample at the median intrinsic (i.e. dust corrected) UV magnitude ($M_{UV} = -21.8$), into UV-faint (median $M_{UV} = -21.3$) and UV-bright (median $M_{UV} = -22.4$) subsamples, spanning intrinsic UV luminosities in the range of $0.05 \lesssim (L_{UV}/L^*_{UV}) \lesssim 2.5$. The maximum likelihood fitting technique returned values of $\langle f_{esc} \rangle = 0.18^{+0.06}_{-0.05}$ for the UV-faint galaxies and $\langle f_{esc} \rangle = 0.03^{+0.02}_{-0.01}$ for the UV-bright galaxies (Fig. 9). The constraints returned by the Bayesian inference approach are consistent, with $\langle f_{esc} \rangle = 0.10^{+0.04}_{-0.03}$ and $\langle f_{esc} \rangle = 0.04^{+0.01}_{-0.01}$, respectively (Fig. 10). We note that the decision to focus on the intrinsic UV magnitude rather than observed UV magnitude was taken because the latter is heavily dust-attenuation dependent, especially at the bright end, complicating the physical interpretation.

A summary of the $\langle f_{esc} \rangle$ constraints for the full galaxy sample and the four sample splits considered here is presented in Table 1. The constraints derived from the two fitting approaches are consistent to at least the 2σ level, across all sample splits investigated. Taken together, these results form a consistent picture, in which LyC

Table 1. Summary of the best-fitting $\langle f_{esc} \rangle$ values of the various samples discussed in Section 4. Results are quoted for both the maximum likelihood and Bayesian inferences methods. Upper limits represent 2σ constraints.

Sample	Maximum likelihood	Bayesian inference
Full sample	$0.07^{+0.02}_{-0.02}$	$0.05^{+0.01}_{-0.01}$
Low $W_\lambda(Ly\,\alpha)$	$0.02^{+0.02}_{-0.02}$	<0.03
High $W_\lambda(Ly\,\alpha)$	$0.12^{+0.06}_{-0.04}$	$0.08^{+0.02}_{-0.02}$
Red β	$0.04^{+0.01}_{-0.02}$	<0.03
Blue β	$0.22^{+0.04}_{-0.06}$	$0.14^{+0.06}_{-0.04}$
High $M_\star$	$0.06^{+0.02}_{-0.02}$	$0.05^{+0.02}_{-0.01}$
Low $M_\star$	$0.09^{+0.05}_{-0.04}$	$0.05^{+0.02}_{-0.01}$
Intrinsic UV bright	$0.03^{+0.02}_{-0.01}$	$0.04^{+0.01}_{-0.01}$
Intrinsic UV faint	$0.18^{+0.06}_{-0.05}$	$0.10^{+0.04}_{-0.03}$

photons preferentially escape from the same UV-faint, dust-free galaxies that are also the primary sources of Lyα escape. Across the range of physical properties probed by our sample, the typical escape fraction appears to roughly encompass $f_{esc} \simeq 0-0.2$, with a full sample average of $\langle f_{esc} \rangle \simeq 0.07$. While our current sample is limited in terms of statistics and dynamic range, our analysis clearly demonstrates the ability of our adopted technique to recover $\langle f_{esc} \rangle$ trends from broad-band photometry.

4.4 Individual $\mathcal{R}_{obs}$ detections

The analysis presented here is primarily focused on constraining $\langle f_{esc} \rangle$ for our galaxy sample based on modelling the shape of the
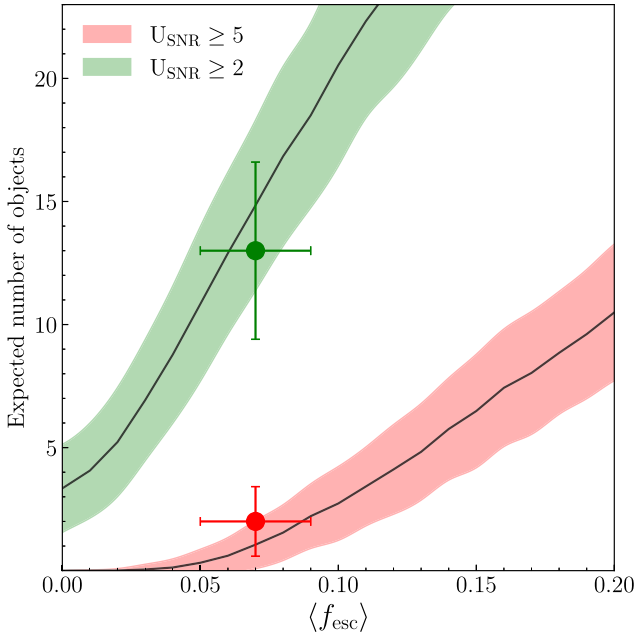
Figure 11. The expected number of *U*-band flux detections in our sample as a function of $\langle f_{esc} \rangle$ (see Section 4.4). The expected number of *U*-band flux detections at $\geq 2\sigma$ and $\geq 5\sigma$ based on our model are shown as the solid black lines, with the 1σ uncertainties indicated by the shaded regions. The two data points indicate the observed number of $\geq 2\sigma$ and $\geq 5\sigma$ detections in our final sample. It can be seen that for our best-fitting value of $\langle f_{esc} \rangle \simeq 0.07$, the expected and observed number of *U*-band flux detections are in good agreement.

$\mathcal{R}_{obs}$ distribution. However, it is worth noting that two objects in our sample could be considered as robust LyC detections, having individual *U*-band flux measurements with $\geq 5\sigma$ significance. Both of these objects have been previously reported in the literature (Vanzella et al. 2010b; Ji et al. 2020; Saxena et al. 2022).

In fact, the number of objects within our sample with a positive *U*-band flux detection provides a useful additional sanity check on the $\langle f_{esc} \rangle$ value we derived for the full sample. We performed a simple test in which we constructed simulated samples as a function of average escape fraction, using the method described in Section 3. For each value of $\langle f_{esc} \rangle$ in the range $0 \leq \langle f_{esc} \rangle \leq 0.2$ ($\Delta \langle f_{esc} \rangle = 0.01$), we produced 5000 simulated samples of 148 galaxies, and calculated the predicted number of *U*-band flux detections. As can be seen from Fig. 11, the number of $\geq 2\sigma$ and $\geq 5\sigma$ *U*-band flux detections we see in the real data is in good agreement with the model prediction for $\langle f_{esc} \rangle = 0.07 \pm 0.02$.

5 DISCUSSION

The results presented above clearly demonstrate that meaningful constraints on $\langle f_{esc} \rangle$ at $z \simeq 3-4$ can be obtained from broad-band photometric measurements of the emergent LyC flux in the *U* band. In this section, we begin by comparing our results to previous measurements in the literature at similar redshifts, before briefly considering the physical picture suggested by our results. We finish with a quantitative discussion of the various systematic uncertainties present in our study, suggesting avenues for future improvement.

5.1 Literature comparison

In Fig. 12, we show a comparison between the $\langle f_{esc} \rangle$ constraints presented in this work and a selection of comparable studies of star-
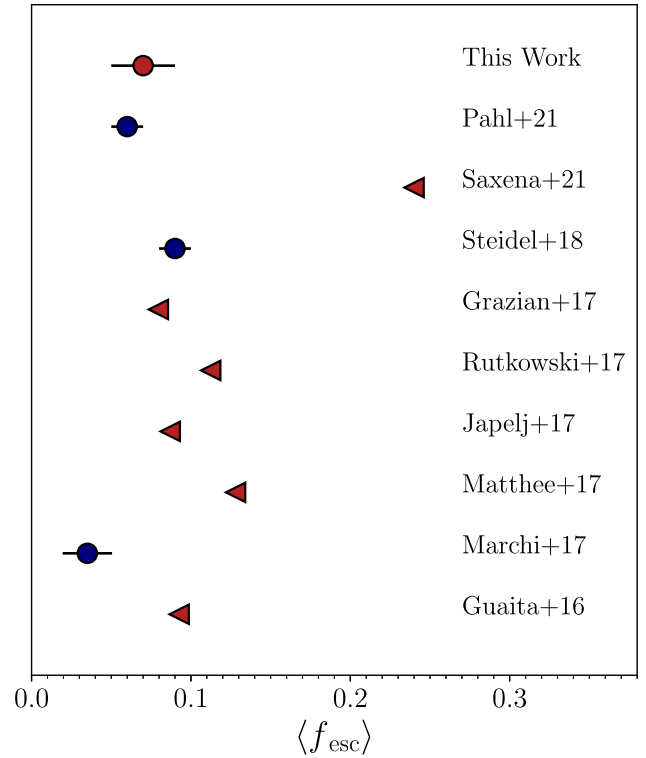

Figure 12. A comparison between the results presented here and $\langle f_{esc} \rangle$ measurements for $z \simeq 3$ galaxy samples in the literature. Results based on photometry are shown in red and results based on spectroscopy are shown in blue. The circular markers represent studies that report a $\geq 2\sigma$ constraint on $\langle f_{esc} \rangle$, while the triangular markers represent studies that report upper limits (2σ). Where necessary, we have converted relative escape fraction estimates to absolute escape fraction estimates assuming $E(B-V) = 0.1$ and the Calzetti et al. (2000) attenuation curve, as in Meštrić et al. (2021). For Grazian et al. (2017), who derive constraints on $\langle f_{esc} \rangle$ as a function of M_{UV}, we plot the result for their $M_{UV} \sim -19.7$ stack, closest to the median of our sample ($M_{UV} \sim -20.2$).

forming galaxies at $z \sim 2-4$ from the literature. The literature compilation includes estimates of $\langle f_{esc} \rangle$ derived from both spectroscopy and photometry. It can be seen that, prior to this work, the only statistical ($\geq 3\sigma$) measurements of $\langle f_{esc} \rangle$ have come from deep spectroscopic analyses (e.g. Marchi et al. 2017; Steidel et al. 2018; Pahl et al. 2021).

The relative success of spectroscopic studies versus photometric studies indicated by Fig. 12 is primarily due to the fact that spectroscopy enables a measurement of the LyC flux across a narrow bandpass, close to the intrinsic Lyman limit, where the optical depth to H I is minimized (e.g. the $880-910$ Å window used by Steidel et al. 2018). For example, at $z = 3.6$, the average IGM + CGM transmission integrated across the *U*-band filter is $\langle e^{-\tau_U^{HI}} \rangle = 0.07$, compared to an average of $\langle e^{-\tau_{900}^{HI}} \rangle = 0.28$ across the $880-910$ Å bandpass.

Despite this, the analysis presented here clearly demonstrates that it is possible to derive constraints from broad-band imaging that move beyond upper limits, and are comparable to those achieved from spectroscopy. However, to achieve this, large statistical samples, ultra-deep *U*-band imaging, accurate treatment of the IGM + CGM optical depth, and an analysis that exploits the full $\mathcal{R}_{obs}$ distribution, are all required.

It can be seen from Fig. 12 that our best-fitting value of $\langle f_{esc} \rangle = 0.07 \pm 0.02$ is fully consistent with the latest estimates from the VIMOS Ultra Deep Survey presented in Marchi et al. (2017), and the

Keck Lyman Continuum Spectroscopic Survey presented in Steidel et al. ([2018](#)) and Pahl et al. ([2021](#)). Moreover, these results are in quantitative agreement with the majority of previous upper limits reported from broadband imaging studies, which typically find $\langle f_{\rm esc}\rangle$ $\lesssim 0.1$ at the 2σ level.

5.2 A physical picture

Our results point towards a surprisingly simple physical picture, in which the observed distribution of the ionizing to non-ionizing UV flux ratio for our galaxy sample can be modelled as population with a single value of $\langle f_{\rm esc}\rangle = 0.07 \pm 0.02$. However, we have also found evidence that $\langle f_{\rm esc}\rangle$ varies as a function of galaxy properties; increasing with $W_{\lambda}({\rm Ly}\,\alpha)$ and decreasing with UV dust attenuation and intrinsic UV luminosity. These trends are in good agreement with recent results from spectroscopic studies at similar redshifts (Steidel et al. [2018](#); Pahl et al. [2021](#)), and have a number of important implications. Most importantly, our result suggest that low-dust, UV-faint galaxies at $z \geq 6$ are plausibly capable of displaying the $\langle f_{\rm esc}\rangle \geq 0.1$ required to drive reionization (Robertson et al. [2013](#); Finkelstein et al. [2019](#)).

As far as our sample is concerned, it is clear from Figs [5](#) and [11](#) that the observed data is fully consistent with our simple model. Indeed, based on our sample alone, there is no indication that the more complex pictures that have been suggested in the literature, in which LyC continuum emission is switched either 'on' or 'off' due to anisotropic dust/ISM distributions leading to line-of-sight effects, and/or stochastic star-formation histories (e.g. Fletcher et al. [2019](#)), are required to explain the data.

However, although our current sample does not justify a more complex physical model statistically, it is clear that the true underlying $f_{\rm esc}$ distribution is likely to be significantly more complicated. In the future, larger sample sizes and deeper photometry should make it possible to fit more complex underlying $f_{\rm esc}$ distributions and quantitatively compare them to our simple model using Bayesian model selection techniques.

Interestingly, in contrast to the clear correlations between $f_{\rm esc}$ and $W_{\lambda}({\rm Ly}\,\alpha)$, β and $M_{\rm UV}$, our results do not show evidence for a strong trend between $f_{\rm esc}$ and galaxy stellar mass. The lack of a clear $f_{\rm esc}-M_{\star}$ trend is perhaps surprising given the known correlations between $M_{\star}$, $W_{\lambda}({\rm Ly}\,\alpha)$, and β (e.g. McLure et al. [2018a](#); Cullen et al. [2020](#)); however, our results suggest while strong Ly α emission, low dust attenuation, and faint intrinsic UV luminosity can be considered primary indicators of $f_{\rm esc}$, any $f_{\rm esc}$ trend with $M_{\star}$, if present, is secondary and 'washed-out' by the scatter in the $M_{\star}-W_{\lambda}({\rm Ly}\alpha)$, $M_{\star}-\beta$, and $M_{\star}-M_{\rm UV}$ relations. This apparent lack of a clear $f_{\rm esc}-M_{\star}$ correlation is in good agreement with recent results for galaxies at $z \simeq 0.4$ reported in Izotov et al. ([2021](#)). However, it is important to note that of the four properties physical properties considered here, $M_{\star}$ is the most model dependent, and therefore subject to the largest number of systematic uncertainties.

Finally, we note that our results are qualitatively in agreement with the results of Reddy et al. ([2016](#)), who found that the ionizing escape fraction is driven predominantly by changes in the covering fraction of H I ($f_{\rm cov}({\rm H\,I})$), with lower $f_{\rm cov}({\rm H\,I})$ corresponding to higher $f_{\rm esc}$ (see also; Gazagnes et al. [2020](#); Reddy et al. [2022](#); Saldana-Lopez et al. [2022](#)). Crucially, Reddy et al. ([2016](#)) showed that dust covering fraction increases with $f_{\rm cov}({\rm H\,I})$, implying that $f_{\rm esc}$ will decrease towards galaxies with lower dust attenuation, consistent with our findings. Indeed, a fundamental correlation between $f_{\rm esc}$ and $f_{\rm cov}({\rm H\,I})$ (or dust) is well-motivated from a theoretical point of view, and naturally explains the resulting $f_{\rm esc}$ trends with $W_{\lambda}({\rm Ly}\,\alpha)$ and β.

5.3 Systematic uncertainties

Before concluding, it is worth considering the systematic impact of some of the key choices made in our analysis and understanding the effect that they have on our results.

One simplifying assumption we made was the choice of a single underlying SPS model for the full sample, which fixes the intrinsic ratio of ionizing to non-ionizing UV flux (Section [3.1](#)). Although this single model is physically motivated, being derived from a full-spectrum fit to the stacked VANDELS spectrum of our full galaxy sample, other choices for the intrinsic underlying SED would systematically alter the value of $\mathcal{R}_{\rm int}$, and hence $\langle f_{\rm esc}\rangle$. However, it is important to note that our choice of the BPASS binary models yields larger values of $\mathcal{R}_{\rm int}$ than most other available SPS models, and in that sense most alternative models would result in marginally larger $\langle f_{\rm esc}\rangle$ estimates. However, this is a relatively small systematic effect, for example, assuming the Starburst99 models (Leitherer et al. [1999](#)), with the same star formation history and IMF, increases $\langle f_{\rm esc}\rangle$ by a factor of $\simeq 1.1$.

We have also assumed constant star-formation histories on a 100 Myr time-scale, a common assumption when modelling the stellar populations of $z \simeq 2-3$ star-forming galaxies (e.g. Steidel et al. [2016](#); Cullen et al. [2019](#)). Alternative choices for the star formation history have only a minor effect on $\mathcal{R}_{\rm int}$ (<10 per cent), as long as the assumption of a constant star-formation rate is valid on time-scales $\gtrsim 50$ Myr. Systematically, younger ages would increase $\mathcal{R}_{\rm int}$ and hence decrease the resulting $\langle f_{\rm esc}\rangle$ (at the $\gtrsim 20$ per cent level). However, there is currently no strong observational evidence for star-formation time-scales <50 Myr at the typical stellar mass of our sample.

Another simplifying assumption we made was to adopt a single dust law, with a slope of $\delta = -0.25$, motivated by a comparison between the intrinsic model and the stacked spectrum of the full sample (Section [3](#)). A $\delta = -0.25$ slope is intermediate between the commonly adopted Calzetti ($\delta = 0$) and SMC curves ($\delta = -0.5$). Adopting a dust curve as steep as the SMC extinction curve would *increase* our derived $\langle f_{\rm esc}\rangle$ values by a factor of $\simeq 1.5$. In contrast, adopting an attenuation curve as grey as the Calzetti et al. ([2000](#)) star-burst law would *decrease* our derived $\langle f_{\rm esc}\rangle$ values by a factor of $\simeq 1.7$.

In reality, each galaxy in our sample has a unique metallicity, star formation history and dust attenuation curve, which could in principle be incorporated directly into the determination of $\langle f_{\rm esc}\rangle$ in a future analysis. Nevertheless, first-order estimates of the potential systematic effects suggest the range of $\langle f_{\rm esc}\rangle$ for the full sample would remain within the range $0.03 \leq \langle f_{\rm esc}\rangle \leq 0.1$.

6 CONCLUSIONS

We have presented the results of a study aimed at constraining the average Lyman-continuum escape fraction $\langle f_{\rm esc}\rangle$ of star-forming galaxies at $z \simeq 3.5$. After performing a careful selection against line-of-sight contamination and AGN interlopers, we assembled a sample of 148 galaxies at $3.35 \leq z_{\rm spec} \leq 3.95$ from the VANDELS spectroscopic survey (McLure et al. [2018b](#); Garilli et al. [2021](#)).

Using a combination of ultra-deep, ground-based, *U*-band imaging and *Hubble Space Telescope V*-band imaging, we were able to robustly measure $\mathcal{R}_{\rm obs} = (L_{\rm LyC}/L_{\rm UV})_{\rm obs}$ for each galaxy. By fitting the $\mathcal{R}_{\rm obs}$ distribution of our full sample, we were able to derive consistent constraints on $\langle f_{\rm esc}\rangle$, using two different fitting techniques. Both techniques were based upon the assumption that a single value of $f_{\rm esc}$ could be applied to the full sample and utilized accurate Monte

Carlo simulations to trace the full distribution of H I optical depths through the intervening IGM and CGM.

Splitting the sample in two, we investigated the evidence for trends between $\langle f_{esc} \rangle$ and a number of physical properties, namely $W_\lambda(Ly\alpha)$, β_{obs}, $M_\star$, and intrinsic M_{UV}. The main results of this study can be summarized as follows:

(i) Fitting the $\mathcal{R}_{obs}$ distribution for the full sample using a maximum-likelihood technique returns a best-fitting value of $\langle f_{esc} \rangle = 0.07 \pm 0.02$ (Fig. 6). Models with $\langle f_{esc} \rangle = 0$ and $\langle f_{esc} \rangle \geq 0.15$ are rejected at the $\geq 3\sigma$ level. Using an independent Bayesian inference approach, we obtain a fully consistent value of $\langle f_{esc} \rangle = 0.05 \pm 0.01$ (Fig. 8). This result represents the first significant measurement ($\geq 3\sigma$) of $\langle f_{esc} \rangle$ from ground-based broadband imaging at $z > 3$.

(ii) Splitting the full sample into sub-samples based on various physical properties, we find evidence that $\langle f_{esc} \rangle$ positively correlates with $W_\lambda(Ly\alpha)$, but anticorrelates with intrinsic UV luminosity and UV dust attenuation. We find that the high $W_\lambda(Ly\alpha)$, low-intrinsic UV luminosity, and low dust attenuation sub-samples all return best-fitting $\langle f_{esc} \rangle$ values in the range $0.12 \leq \langle f_{esc} \rangle \leq 0.22$ (see Figs 9 and 10).

(iii) In contrast, splitting the sample by $M_\star$ yields a weak/non-existent trend between $M_\star$ and f_{esc}. Our results suggest that $M_\star$ is, at best, a secondary indicator of f_{esc}. Therefore, any trend between f_{esc} and $M_\star$ is likely the result of the known correlations between $M_\star$ and the other stronger indicators: $W_\lambda(Ly\alpha)$, β_{obs}, and M_{UV}.

(iv) Overall, the results of the subsample split suggest that the young, low-metallicity, dust-free galaxies expected to be common at $z \geq 6$ are likely to display $\langle f_{esc} \rangle \geq 0.1$, the threshold often quoted as necessary for them to drive cosmic reionization.

(v) The agreement between our simple model and the observed data (Figs 5 and 11) suggests that, at least for our sample, a more complicated model of the underlying f_{esc} distribution is not statistically justified. Nevertheless, it is clear that the true underlying f_{esc} distribution is likely to be significantly more complicated than our simple model. Therefore, it would clearly be desirable to expand the modelling performed here to larger galaxy samples with deeper photometry, in order to explore more complicated f_{esc} distributions and to improve the significance of the correlations between f_{esc} and various galaxy properties.

ACKNOWLEDGEMENTS

DATA AVAILABILITY

The VANDELS survey is a European Southern Observatory Public Spectroscopic Survey. The full spectroscopic data set, together with the complementary photometric information and derived quantities, are available from http://vandels.inaf.it, as well as from the ESO archive https://www.eso.org/qi/. The *U*-band imaging data is also publicly available from the ESO archive, with information found at https://archive.eso.org/cms/eso-data/data-packages/goods-vimos-imaging-data-release-version-1-0.html. The *HST* imaging is publicly available from the Hubble Legacy Fields data release at the STSCI archive from https://archive.stsci.edu/prepds/hlf/#data-products. For the purpose of open access, the author has applied a Creative Commons Attribution (CC BY) licence to any Author Accepted Manuscript version arising from this submission.

REFERENCES

Aird J., Coil A. L., Georgakakis A., Nandra K., Barro G., Pérez-González P. G., 2015, MNRAS, 451, 1892
Asplund M., Grevesse N., Sauval A. J., Scott P., 2009, ARA&A, 47, 481
Astropy Collaboration, 2013, A&A, 558, A33
Astropy Collaboration, 2018, AJ, 156, 123
Bertin E., 2011, in Evans I. N., Accomazzi A., Mink D. J., Rots A. H., eds, ASP Conf. Ser. Vol. 442, Astronomical Data Analysis Software and Systems XX (ADASSXX). Astron. Soc. Pac., San Francisco, p. 435
Bosman S. E. I. et al., 2021, preprint (arXiv:2108.03699)
Bouwens R. J. et al., 2015, ApJ, 803, 34
Bouwens R. J. et al., 2021, AJ, 162, 47
Bowler R. A. A., Jarvis M. J., Dunlop J. S., McLure R. J., McLeod D. J., Adams N. J., Milvang-Jensen B., McCracken H. J., 2020, MNRAS, 493, 2059
Brammer G. B. et al., 2016, ApJS, 226, 6
Calzetti D., Kinney A. L., Storchi-Bergmann T., 1994, ApJ, 429, 582
Calzetti D., Armus L., Bohlin R. C., Kinney A. L., Koornneef J., Storchi-Bergmann T., 2000, ApJ, 533, 682
Carnall A. C., McLure R. J., Dunlop J. S., Davé R., 2018, MNRAS, 480, 4379
Carnall A. C. et al., 2019, MNRAS, 490, 417
Cen R., Kimm T., 2015, ApJ, 801, L25
Chary R., Petitjean P., Robertson B., Trenti M., Vangioni E., 2016, Space Sci. Rev., 202, 181
Cullen F. et al., 2018, MNRAS, 476, 3218
Cullen F. et al., 2019, MNRAS, 487, 2038
Cullen F. et al., 2020, MNRAS, 495, 1501
Cullen F. et al., 2021, MNRAS, 505, 903
Daddi E. et al., 2007, ApJ, 670, 156
de Barros S. et al., 2016, A&A, 585, A51
Dijkstra M., Gronke M., Venkatesan A., 2016, ApJ, 828, 71
Du X. et al., 2018, ApJ, 860, 75
Eldridge J. J., Stanway E. R., Xiao L., McClelland L. A. S., Taylor G., Ng M., Greis S. M. L., Bray J. C., 2017, PASA, 34, e058
Endsley R., Stark D. P., Chevallard J., Charlot S., 2021, MNRAS, 500, 5229
Faisst A. L. et al., 2022, ApJ, 929, 66
Finkelstein S. L. et al., 2015, ApJ, 810, 71
Finkelstein S. L. et al., 2019, ApJ, 879, 36
Fletcher T. J., Tang M., Robertson B. E., Nakajima K., Ellis R. S., Stark D. P., Inoue A., 2019, ApJ, 878, 87
Foreman-Mackey D., Hogg D. W., Lang D., Goodman J., 2013, PASP, 125, 306
Garilli B. et al., 2021, A&A, 647, A150
Gazagnes S., Chisholm J., Schaerer D., Verhamme A., Izotov Y., 2020, A&A, 639, A85
Gordon K. D., Clayton G. C., Misselt K. A., Landolt A. U., Wolff M. J., 2003, ApJ, 594, 279
Goto H. et al., 2021, ApJ, 923, 229
Grazian A. et al., 2017, A&A, 602, A18
Gronke M., Bull P., Dijkstra M., 2015, ApJ, 812, 123
Guaita L. et al., 2016, A&A, 587, A133
Harikane Y. et al., 2022, ApJS, 259, 20
Harris C. R. et al., 2020, Nature, 585, 357
Hunter J. D., 2007, Comput. Sci. Eng., 9, 90
Inoue A. K., Shimizu I., Iwata I., Tanaka M., 2014, MNRAS, 442, 1805
Iwata I. et al., 2022, MNRAS, 509, 1820

Izotov Y. I., Worseck G., Schaerer D., Guseva N. G., Thuan T. X., Fricke Verhamme A., Orlitová I., 2018, MNRAS, 478, 4851

Izotov Y. I., Worseck G., Schaerer D., Guseva N. G., Chisholm J., Thuan T. X., Fricke K. J., Verhamme A., 2021, MNRAS, 503, 1734

Jaskot A. E., Dowd T., Oey M. S., Scarlata C., McKinney J., 2019, ApJ, 885, 96

Ji Z. et al., 2020, ApJ, 888, 109

Kashino D. et al., 2022, ApJ, 925, 82

Katz H. et al., 2020, MNRAS, 498, 164

Kewley L. J., Nicholls D. C., Sutherland R. S., 2019, ARA&A, 57, 511

Kimm T., Cen R., 2014, ApJ, 788, 121

Kornei K. A., Shapley A. E., Erb D. K., Steidel C. C., Reddy N. A., Pettini M., Bogosavljević M., 2010, ApJ, 711, 693

Kroupa P., 2001, MNRAS, 322, 231

Kulkarni G., Worseck G., Hennawi J. F., 2019, MNRAS, 488, 1035

Leitherer C. et al., 1999, ApJS, 123, 3

Luo B. et al., 2017, ApJS, 228, 2

Marchi F. et al., 2017, A&A, 601, A73

Mason C. A., Treu T., Dijkstra M., Mesinger A., Trenti M., Pentericci L., de Barros S., Vanzella E., 2018, ApJ, 856, 2

Mauerhofer V., Verhamme A., Blaizot J., Garel T., Kimm T., Michel-Dansac L., Rosdahl J., 2021, A&A, 646, A80

McGreer I. D., Fan X., Jiang L., Cai Z., 2018, AJ, 155, 131

McLure R. J. et al., 2018a, MNRAS, 476, 3991

McLure R. J. et al., 2018b, MNRAS, 479, 25

Meštrić U. et al., 2020, MNRAS, 494, 4986

Meštrić U., Ryan-Weber E. V., Cooke J., Bassett R., Prichard L. J., Rafelski M., 2021, MNRAS, 508, 4443

Meyer R. A. et al., 2020, MNRAS, 494, 1560

Mostardi R. E., Shapley A. E., Nestor D. B., Steidel C. C., Reddy N. A., Trainor R. F., 2013, ApJ, 779, 65

Naidu R. P., Tacchella S., Mason C. A., Bose S., Oesch P. A., Conroy C., 2020, ApJ, 892, 109

Nakajima K., Ouchi M., 2014, MNRAS, 442, 900

Nakajima K., Ellis R. S., Robertson B. E., Tang M., Stark D. P., 2020, ApJ, 889, 161

Nonino M. et al., 2009, ApJS, 183, 244

Ocvirk P., Lewis J. S. W., Gillet N., Chardin J., Aubert D., Deparis N., Thélie É., 2021, MNRAS, 507, 6108

Pahl A. J., Shapley A., Steidel C. C., Chen Y., Reddy N. A., 2021, MNRAS, 505, 2447

Parsa S., Dunlop J. S., McLure R. J., 2018, MNRAS, 474, 2904

Pentericci L. et al., 2018, A&A, 616, A174

Pérez F., Granger B. E., 2007, Comput. Sci. Eng., 9, 21

Planck Collaboration VI, 2020, A&A, 641, A6

Ramambason L., Schaerer D., Stasińska G., Izotov Y. I., Guseva N. G., Vílchez J. M., Amorín R., Morisset C., 2020, A&A, 644, A21

Reddy N. A., Steidel C. C., Pettini M., Bogosavljević M., Shapley A. E., 2016, ApJ, 828, 108

Reddy N. A. et al., 2018, ApJ, 853, 56

Reddy N. A. et al., 2022, ApJ, 926, 31

Rivera-Thorsen T. E. et al., 2019, Science, 366, 738

Robertson B. E., 2022, ARA&A, 60, in press

Robertson B. E. et al., 2013, ApJ, 768, 71

Robertson B. E., Ellis R. S., Furlanetto S. R., Dunlop J. S., 2015, ApJ, 802, L19

Rudie G. C. et al., 2012, ApJ, 750, 67

Rudie G. C., Steidel C. C., Shapley A. E., Pettini M., 2013, ApJ, 769, 146

Saldana-Lopez A. et al., 2022, preprint (arXiv:2201.11800)

Salim S., Boquien M., Lee J. C., 2018, ApJ, 859, 11

Saxena A. et al., 2022, MNRAS, 511, 120

Shapley A. E., Steidel C. C., Strom A. L., Bogosavljević M., Reddy N. A., Siana B., Mostardi R. E., Rudie G. C., 2016, ApJ, 826, L24

Shivaei I. et al., 2020, ApJ, 899, 117

Siana B. et al., 2015, ApJ, 804, 17

Stanway E. R., Eldridge J. J., 2018, MNRAS, 479, 75

Steidel C. C., Strom A. L., Pettini M., Rudie G. C., Reddy N. A., Trainor R. F., 2016, ApJ, 826, 159

Steidel C. C., Bogosavljević M., Shapley A. E., Reddy N. A., Rudie G. C., Pettini M., Trainor R. F., Strom A. L., 2018, ApJ, 869, 123

Tang M., Stark D. P., Chevallard J., Charlot S., 2019, MNRAS, 489, 2572

Tang M., Stark D. P., Chevallard J., Charlot S., Endsley R., Congiu E., 2021, MNRAS, 503, 4105

Tang M., Stark D. P., Ellis R. S., Charlot S., Feltre A., Shapley A. E., Endsley R., 2022, MNRAS, 509, 3102

Tanvir N. R. et al., 2019, MNRAS, 483, 5380

Tepper-García T., 2006, MNRAS, 369, 2025

Vanzella E., Siana B., Cristiani S., Nonino M., 2010a, MNRAS, 404, 1672

Vanzella E. et al., 2010b, ApJ, 725, 1011

Vanzella E. et al., 2012, ApJ, 751, 70

Vanzella E. et al., 2016a, ApJ, 821, L27

Vanzella E. et al., 2016b, ApJ, 825, 41

Vanzella E. et al., 2018, MNRAS, 476, L15

Vanzella E. et al., 2022, A&A, 659, A2

Verhamme A., Orlitová I., Schaerer D., Hayes M., 2015, A&A, 578, A7

Virtanen P. et al., 2020, Nature Methods, 17, 261

Whitaker K. E. et al., 2019, Astrophys. J. Suppl. Ser., 244, 16

Wise J. H., Demchenko V. G., Halicek M. T., Norman M. L., Turk M. J., Abel T., Smith B. D., 2014, MNRAS, 442, 2560

Wu X., McQuinn M., Eisenstein D., Iršič V., 2021, MNRAS, 508, 2784

APPENDIX: DETAILS OF THE IGM + CGM OPACITY MODELS

To generate our IGM + CGM Monte Carlo models, we adopted the parametrization for the column density and redshift distribution of H I clouds outlined in Steidel et al. (2018). In this prescription, the number of absorbers of column density between $N_{H I, max}$ and $N_{H I, min}$, and redshift between $z1$ and $z2$, is given by

$$N_{abs} = \int_{N_{H I, min}}^{N_{H I, max}} \int_{z1}^{z2} N_{H I}^{-\beta} A(1+z)^{\gamma} dN_{H I} dz, \qquad (A1)$$

where β and γ are power-law exponents describing the column destiny and redshift distribution of the number of absorbers and A is a constant chosen to match the observations of Rudie et al. (2013) for galaxies in the redshift range $2.0 \lesssim z \lesssim 2.8$. The distributions are split into three regimes: low-density IGM, high-density IGM, and CGM, with the relevant parameters for each regime given in table 11 of Steidel et al. (2018).

To generate sightlines at a given redshift, absorbers within the column density range $12 < \log(N_{H I}) < 21$ were drawn randomly from the appropriate distribution function. For an absorber with column density $N_{H I}$ and Doppler parameter v_D, the optical depth as a function wavelength is given by

$$\tau(\lambda) = N_{HI} \left[\sigma_{LyC}(\lambda) + \sum \sigma_i(\lambda) \right], \qquad (A2)$$

where $\sigma_{LyC}(\lambda)$ is the absorption cross-section of the Lyman continuum and $\sigma_i(\lambda)$ is the absorption cross-section of the ith Lyman series line. The cross-section for the Lyman continuum is approximated to

$$\sigma_{LyC} \simeq 6.3 \times 10^{-18} \left(\frac{\lambda}{\lambda_{LyC}} \right)^3, \qquad (A3)$$

where $\lambda \leq \lambda_{LyC}$ (i.e. when $\lambda > \lambda_{LyC}$, $\sigma_{LyC} = 0$).

Following Tepper-García (2006), the cross-section for a given line in the Lyman series is given by

$$\sigma_i(\lambda) = \kappa_i H[a_i, x] \quad [cm^2], \qquad (A4)$$

where

$$\kappa_i = \frac{\sqrt{\pi} e^2 \lambda_i^2 f_i}{m_e c^2 \Delta \lambda_D} \quad [cm^2], \qquad (A5)$$

where f_i is the oscillator strength of the strength of the transition, λ_i is the wavelength of the transition in cm. Note that the units here are in the cgs system (e.g. $e = 4.803 \times 10^{-10}$ Fr, $m_e = 9.109 \times 10-28$ g; $c = 2.998 \times 10^{10}$ cms^{-1}). $\Delta\lambda_D$ is the Doppler width of the line given by

$$\Delta\lambda_D = \frac{v_D}{c}\lambda_i. \tag{A6}$$

$H[a_i, x]$ is the Voigt–Hjerting profile that describes the shape of the line, the analytic approximation to this function given by Tepper-García ([2006]) is

$$H[a_i, x] = H_0 - a_i/\sqrt{\pi}/x^2[H_0^2(4x^2x^2 + 7x^2$$
$$+4 + Q) - Q - 1], \tag{A7}$$

where $x = (\lambda - \lambda_i)/\Delta\lambda_D$, $H_0 \equiv e^{-x^2}$, and $Q \equiv 1.5/x^2$. The dimensionless damping parameter a_i is given by

$$a_i = \frac{\lambda_i^2\Gamma_i}{4\pi c\Delta\lambda_D}, \tag{A8}$$

where Γ_i is the damping constant, or the reciprocal of the mean lifetime of the transition. The atomic data for the Lyman series transitions were taken from the NIST Atomic Spectra Database[5] and we calculated up to the 40th transition.

---

[5]https://physics.nist.gov/PhysRefData/ASD/lines_form.html.

This paper has been typeset from a TeX/LaTeX file prepared by the author.